Relating hydro-mechanical and elastodynamic properties of dynamically-stressed tensile-fractured rock in relation to fracture aperture and contact area

Clay E. Wood[1], Prabhakaran Manogharan[2], Andy Rathbun[3], Jacques Rivière[2], Derek Elsworth[4,1], Chris Marone[1,5], Parisa Shokouhi[2]

[1]Dept. of Geosciences, Pennsylvania State University, University Park, PA 16802, USA
[2]Dept. of Engineering Science and Mechanics, Pennsylvania State University, University Park, PA 16802, USA
[3]Chevron ETC, San Ramon, CA 12345, USA
[4]Dept. of Energy and Mineral Engineering, EMS Energy Institute, and G3 Center, The Pennsylvania State University, University Park, PA, USA
[5]Dipartimento di Scienze della Terra, La Sapienza Università di Roma

Key Points:

- Lab experiments simulate conditions representative of fractures at various depths, stresses, under dynamic stressing
- Simultaneous measurements of fluid flow and active-source ultrasonic transmission show how these mechanisms are coupled
- Local fracture aperture, not necessarily the stress state, dominate elastic and hydraulic responses to dynamic stressing

Corresponding author: Clay Wood, `cew52@psu.edu`

Abstract

We exploit nonlinear elastodynamic properties of fractured rock to probe the micro-scale mechanics of fractures and understand the relation between fluid transport and fracture aperture and area, stiffness proxy, under dynamic stressing. Experiments are conducted on rough, tensile-fractured Westerly granite specimen subject to triaxial stresses. Fracture permeability is measured from steady-state fluid flow with deionized water. Pore pressure oscillations are applied at amplitudes ranging from 0.2 to 1 MPa at 1 Hz frequency. During dynamic stressing we transmit acoustic signals through the fracture using an array of piezoelectric transducers (PZTs) to monitor the evolution of fracture interface properties. We examine the influence of fracture aperture and contact area by conducting measurements at effective normal stresses of 10, 12.5, 15, 17.5, and 20 MPa. Additionally, the evolution of contact area with stress is characterized using pressure sensitive film. These experiments are conducted separately with the same fracture and they map contact area at stresses from 9 to 21 MPa. The resulting 'true' area of contact measurements made for the entire fracture surface and within the calculated PZT sensor footprints, numerical modeling of Fresnel zone. We compare the elastodynamic response of the the fracture using the stress-induced changes ultrasonic wave velocities for a range of transmitter-receiver pairs to image spatial variations in contact properties, which is informed by fracture contact area measurements. These measurements of the nonlinear elasticity are related to the fluid-flow, permeability, in response to dynamic stressing and similar comparisons are made for the slow-dynamics, recovery, of the fracture interface following the stress perturbations.

Plain Language Summary

We perform laboratory experiments with fractured rock to understand the relation between fluid flow, fracture openness, and elastic properties under oscillating stressing. These experiments are conducted on rough, pre-fractured granite specimens under stress conditions similar to those found in the shallow earth, a few kilometers in depth. Fluid pressure in the fracture is oscillated at various amplitudes at a fixed frequency. During this dynamic stressing, we use an ultrasonic device to monitor the evolution of the fracture interface. We examine the influence of fracture aperture and contact area by conducting measurements at increasing stress state. Additionally, the evolution of contact area with stress is characterized using pressure sensitive film, showing an image of where the two halves of the fracture are in contact. The ultrasonic monitoring reveals spatial variations in contact properties, which is informed by fracture contact area measurements. These measurements are also related to the fluid-flow in response to dynamic stressing and similar comparisons are made for how the fracture interface evolves, recovers, following the stress perturbations.

1 Introduction

During the course of industrial activities of hydrocarbon recovery or sequestration of carbon or wastewater (pumping, injection, and supercritical H_2O–CO_2 fluids transport) are likely dominant factors in injection-induced seismicity (Healy et al., 1968; Raleigh et al., 1976; Simpson et al., 1988; Sminchak & Gupta, 2003; McNamara et al., 2015; McGarr et al., 2015; Walsh & Zoback, 2015). These industrial activities may produce dynamic perturbations in the local stress field of the subsurface, resulting in changes in poromechanical properties, potentially reactivating fault slip. The poromechanical response of faults, fractured rock, are similarly influenced by dynamic stressing from anthropogenic (industrial) and natural (elastic waves from earthquakes), indicating that these mechanisms – elastic softening and fluid transport – are correlated. In this work we seek to decouple the nonlinear elastic and fluid flow responses to dynamic stressing.

Field and laboratory observations demonstrate that elastic waves propagating from earthquakes may manifest transient changes of the elastic properties in fault zones. Observations form the field document a co-seismic softening, an instantaneous wave speed decrease, followed by a time-logarithmic post-seismic recovery of the fractured rock stiffness e.g., (Brenguier et al., 2008). Laboratory experiment implementing dynamic acoustoelastic testing (DAET) (Shokouhi et al., 2017), show that transmitted ultrasonic wave velocity decreases in response to stress oscillations followed by a time logarithmic recovery. Recently, DAET is used to study the nonlinear elastodynamic response of fractured rock under different stress and saturation conditions (Manogharan et al., 2021). In these studies, the nonlinear elastic responses can be activated with dynamic strains on the order of 10^{-6} (Guyer & Johnson, 2009; Rivière et al., 2015). The nonlinear elastodynamic behavior of rock, intact or fractured, is modulated by minute features such as apertures (governing flow transport, asperity compliance) and higher-order effects such as nonlinear effective stiffness (impacted by rate and state-dependent friction and healing).

Dynamic strain perturbations propagating as elastic waves from earthquakes may induce pore pressure oscillations sufficiently large enough to change permeability (Brodsky & Lajoie, 2013). This may even perturb fault stability (Boettcher & Marone, 2004; Savage & Marone, 2007; P. A. Johnson et al., 2016) thus triggering seismicity (Brodsky & Lajoie, 2013; van der Elst et al., 2013).The underlying mechanism dominating empirical observations of permeability enhancement (and reduction) is postulated to be mobilizing and arresting of particles in porous media (Roberts, 2005; Roberts & Abdel-Fattah, 2009; Liu & Manga, 2009; Elkhoury et al., 2011; Candela et al., 2014, 2015). This effect of clogging and unclogging of pore throats has been observed experimentally (Elkhoury

et al., 2011; Candela et al., 2014), but the relation between these observations and elastic properties of fractured rock is not well understood.

Decoupling the hydro-mechanical and nonlinear elastodynamic properties of fractured rock is crucial for understanding consequences of dynamic stresses in the subsurface, especially at faults. Empirical studies, laboratory, investigating this relationship are currently limited to (Shokouhi et al., 2020; Wood et al., 2021). Here, we show results from complex laboratory experiments in which we combine the analysis of nonlinear elastodynamic and fluid transport data of a tensile-fractured specimen of Westerly granite subject to pore pressure perturbations. A unique contribution of this study is combining the aforementioned analysis with measurements of fracture asperity deformation including spatial variability.

2 Experimental Setup

We conducted a series of highly-constrained laboratory experiments on a pre-fractured sample of Westerly granite. For the first experiment (p5483), nonlinear elastic properties and flow rate were measured simultaneously under true triaxial stresses. In the following experiments (p5595 and p5596), the real area of contact on the fracture was estimated as a function of normal stress. The sample was cut into a L-shaped block 69 x 45 x 50 x 26 mm (Figure 1a-b) that we grooved along the perimeter and split in Mode I over a knife-edge to create a rough quasi-planar fracture. The pre-fractured sample was re-mated, placed between two loading platens, and then sealed with a latex membrane (separating pore fluid from confining fluid). The steel loading platens include embedded piezoelectric transducers (PZTs) as well as internal conduits to provide a distributed line source of fluid at both ends of the fracture, Figure 1b (using a modified version of the method of (Elkhoury et al., 2011)). After extensive preparation, the sample was placed inside a pressure vessel, Figure 1c-d. Each loading axis is independently servo-controlled, including upstream and downstream fluid flow from pressure intensifiers. Mechanical displacements and stresses are measured with direct current displacement transducers (Trans-Tek Series 240 DCDT) as well as custom-built load cells and recorded by a 24-bit analog-to-digital data acquisition system at 100 Hz. Active source ultrasonic monitoring was conducted using a Vantage^{TM} Research Ultrasound (Verasonics) system and PZTs (APC International Ltd. 6.35 mm diameter compressional crystals) with a nominal center frequency of 500 kHz. The transmitting PZTs were pulsed every 0.2 ms and the ultrasonic response is recorded at the receiving PZTs at 25 MHz. A triggering signal from the Verasonics system is also recorded by the mechanical data acquisition system, allowing data synchronization. More details for the data acquisition are found in (Shokouhi et al., 2020; Manogharan et al., 2021; Wood et al., 2021).

Experiment	Description
p5483	Pp oscillation @ [10, 12.5, 15, 17.5, 20] MPa NS
p5595	Pressure sensitive film in horizontal configuration
p5596	Pressure sensitive film in vertical configuration

Table 1. Details of experiments used in this study.

2.1 Experimental Procedure

After sample preparation and installation into the pressure vessel, the experiment commenced with the application of a normal stress of $\sim$ 10 MPa followed by a confining pressure of $\sim$ 5 MPa. Next, the inlet (P_{pA} = 2.5 MPa) and outlet (P_{pB} = 1.5 MPa)

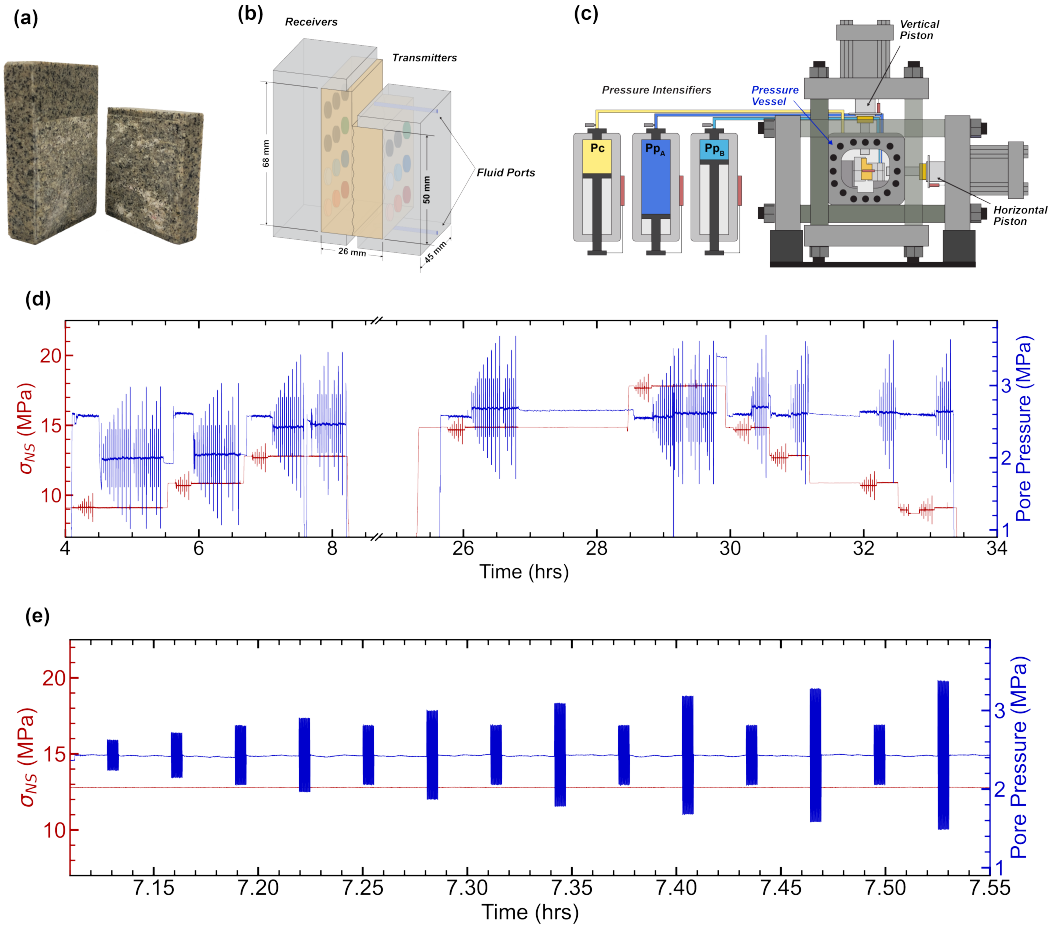

Figure 1. (a) Pre-fractured L-shaped Westerly granite sample. (b) Transmitter-receiver pairs used in active source ultrasonic monitoring embedded inside loading blocks (inactive sensors are dark-grey). (c) Biaxial loading apparatus with pressure vessel in Penn State's Rock Mechanics Laboratory. After the sample was prepared and installed in the pressure vessel, the fracture was saturated with deionized water. Imposed dynamic oscillations of pore pressure with amplitudes ranging from 0.2 to 1 MPa at 1 Hz. (d) Overview of the experiment showing the applied normal stress levels (10, 12.5, 15, 17.5, 20 MPa) in red and pore pressure oscillations in blue. (e) Pore pressure oscillations at 15 MPa σ_{eff}.

pressures were applied to provide a pressure differential across the sample, Figure 1. The large difference in confining and pore fluid pressures prevents fluid from flowing around the outside of the sample and/or along the grooved contour around the sample (used during tensile fracture). Pore pressure oscillations were applied via servo control by feeding a sinusoidal command signal to the inlet pressure intensifier P_{pA}. P_p stress oscillations ranged in amplitude from 0.2 to 1 MPa at 1 Hz while holding P_{pB} constant, Figure 1d. Afterward, the effective stress state was increased for a total of 5 different stress levels [10, 12.5, 15, 17.5, 20] MPa. Due to experimental constraints, the effective stress state was decreased to ∼1 MPa and held over several hours, before resuming the experiment at 17.5 MPa. Three sets of pore pressure oscillations of varying amplitudes were repeated three times at each normal stress level when stresses were incremented and four sets when decremented, Figure 1d - e. The decremental stress levels, [17.5, 15, 12.5, 10] MPa, were conducted in order immediately proceeding largest stress, 20 MPa, and with an hour

hold at 12.5 MPa. This protocol is designed to investigate the repeatability of measurements and to determine the effect, if any, of loading and unloading on the fracture properties (elastic nonlinearity, permeability).

2.2 Permeability Measurement

Independent measurements of volumetric inflow (Q_A) and outflow (Q_B) rates are made using Linear Variable Differential Transformers (LVDTs) attached to the pistons of the pressure intensifiers. Our flow rate measurements are continuous, but we only consider data for near-steady flow conditions ($Q_A - Q_B \leq 5\%$). Darcy's law is used to calculate permeability k:

$$k = \frac{\mu \, L \, Q}{S \, \Delta P_P} \tag{1}$$

where $Q = \frac{1}{2}(Q_A + Q_B)$ is the average flow rate, μ is the fluid viscosity (10^{-3} Pa·s) at 20° C, L is the length of the flow path along the fracture plane (50 mm) and S is the cross-sectional area perpendicular to the flow path (45 mm × 26 mm), which includes both the fracture and granite wall rock. This gives a bulk measure of permeability including the fracture and surrounding rock matrix ($k \sim 10^{-21}$ m^2). The permeability could also be calculated using other valid approaches (F. Zhang et al., 2017; Ishibashi et al., 2018) which isolate the fracture permeability, but our focus here is on relative *changes* in permeability dominated by the stress-sensitive fracture.

3 Active Source Ultrasonic Measurements

Active source ultrasonic data are continuously recorded before, during and after the pore pressure oscillations. P-wave transmitting PZTs are excited with half-sine pulses at 96 V having a center frequency of 500 kHz. Having an array of transmitters and receivers allows us to capture the spatial variability of the fracture's elastodynamic properties (i.e., wave speed and amplitude). Various limitations prevented the use of all possible transmitter-receiver pairs; we report the results from 7 transmitter-receivers pairs. The ultrasonic data are processed as previously documented (Rivière et al., 2013; Manogharan et al., 2021; Wood et al., 2021), where all waveforms are cross-correlated with a reference waveform (constructed by averaging 50 recorded waveforms at the beginning of each experimental run before stress oscillations) to determine a time shift. Since the time shift is typically smaller than the signals' sampling time, often on the order of 1 ns, the resolution is improved with a second-order polynomial fit to the peak of the cross-correlation function. Absolute arrival time is obtained by adding the relative time shift to the p-wave arrival time of the reference waveform (obtained using a threshold). To obtain (corrected) p-wave wave speed, the corrected sample thickness (corrected for compaction/dilation from internal DCDT) is divided by the absolute arrival times. The RMS amplitude is calculated over an approximately 10 μs time window including the p-wave arrival and one full period of the waveforms.

3.1 Fresnel Zone Imaging

A key aim of this study is relating p-wave velocity and permeability changes to changes in the fracture area. To accomplish this, we need to determine the size of the fractured region probed by a given ultrasonic transmitter-receiver pair in our experimental configuration. It is common to implement ray theory approximations of acoustic wave propagation for active-source monitoring that connects changes in wave velocity and amplitude to changes in experimental fault contact area (Hedayat et al., 2014; Shreedharan et al., 2021), for example. In this approximation, waves propagating from source to receiver are considered to be in the high-frequency limit and thus the wavefield is collapsed into a ray path approximated as an infinitesimally thin line (Spetzler & Snieder, 2004). In reality, elastic waves propagate within a finite volume whose width is frequency-dependent,

rather than the volumeless trajectory of a ray path. The region around the propagation trajectory responsible for diffraction in a medium is called the Fresnel zone or Fresnel volume. The region around a ray that mostly influences the propagation of a band-limited wave is called the first Fresnel zone. Previous studies estimated the ellipsoidal Fresnel volume for active-source monitoring (Y. Zhang et al., 2015) by assuming point sources for transmitters and receivers, which may underestimate the region or volume probed by finite-sized transducers.

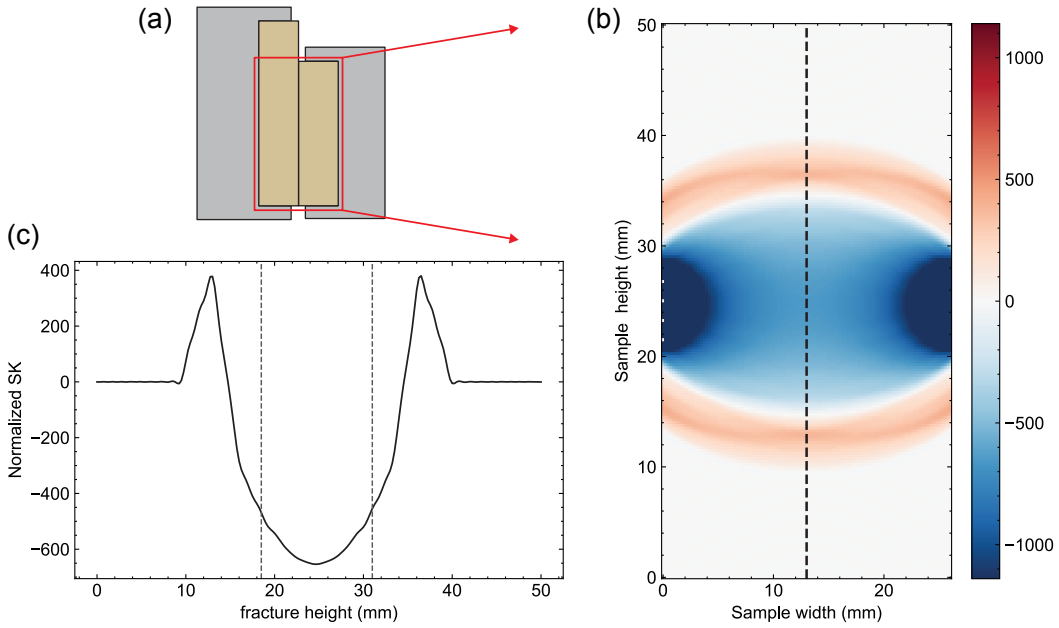

Figure 2. (a) Diagram of L-shaped configuration with region of interest outlined in red. (b) Amplitude sensitivity kernel model across granite block, where intensity represents response of transmitted wave to perturbation. (c) Profile of sensitivity kernel along the fracture plane (denoted by dashed black line in (b)). Dashed gray vertical lines indicate the half-power bandwidth of the Fresnel zone, where the transmitted waves are most sensitive to perturbations along the travel path (left to right).

Here, we numerically model the Fresnel zone resulting from our finite-sized transmitter-receiver PZTs through the bulk rock sample using a sensitivity kernel (SK) to later estimate perturbations in the wavefield amplitude resulting from heterogeneities at the fracture interface. The SK also provides insight on how other types of diffractors, i.e. wave speed or density, affect acoustic wave propagation (Roux et al., 2013). The SK in Figure 2b shows the variation in transmitted wave field amplitude, where red colors indicate increased amplitude and blue colors correspond to reduced relative amplitude (from scattering). It is important to note that in our model we treat our transmitter and receiver as a collection of point sources and consequently the Fresnel zone is a superposition of their respective wavefields. The relative transmitted wave amplitude sensitivity kernel along the fracture profile is shown in Figure 2c, where the width of the half-power bandwidth of the first Fresnel zone (blue) is delineated by dashed gray lines. For a given transducer pair, we consider this region within the Fresnel zone to substantially contribute to the recorded changes in transmission characteristics along the transmitter-receiver travel path.

4 Fracture Contact Characterization

After conducting the dynamic stressing experiment described above, we conducted two additional multi-step experiments to characterize the real area of contact for the tensile fracture specimen under load (p5595 and p5596, see Table 1). This was accomplished by inserting Fuji Prescale© Medium Film (1400 - 7100 psi) between the two halves of the fracture and loading the specimen to a range of stresses. The pressure sensitive film was removed and replaced after each step. Mating the fracture repeatably is imperative for the integrity of the asperities and also for accurate registration of contacts and voids. To that end, we installed locating pins to ensure that the fracture closed consistently each time and that the films were located precisely relative to one another. The pins were installed by drilling two 1.588 mm diameter through-holes in the shorter sample half and blind holes in the taller half such that the locating pins could be inserted to ensure alignment (Figure 3a). A blank pressure sensitive film was cut to size and then inserted between the two fracture halves before loading to the desired target stress. This procedure was repeated with a new pressure sensitive film for each stress ranging from 9 to 21 MPa in increments of 1 MPa. Figure 3b depicts a representative pressure sensitive film loaded to 10 MPa; magenta color corresponds to regions of the fracture interface in contact and the remaining areas are void space. The pressure sensitive films are digitized using a Epson Perfection 3200 Photo color scanner at 3200 dpi resolution. Digitized scans are aligned using cross-correlation (with the lowest stress, 9 MPa, as the reference) and then binarized using an algorithm that generates a threshold value based on mean pixel intensity. Figure 3c show an overlay of the fracture contacts (shades of blue) for 10, 15, and 20 MPa (data from experiment p5596). Note that in experiment p5595, the sample was loaded horizontally, i.e., in the same configuration as in experiment p5483, whereas for experiment p5596, the entire setup was rotated 90°and the sample was loaded in the vertical direction. Loading the sample in the vertical direction greatly helped with properly aligning the two halves of the sample.

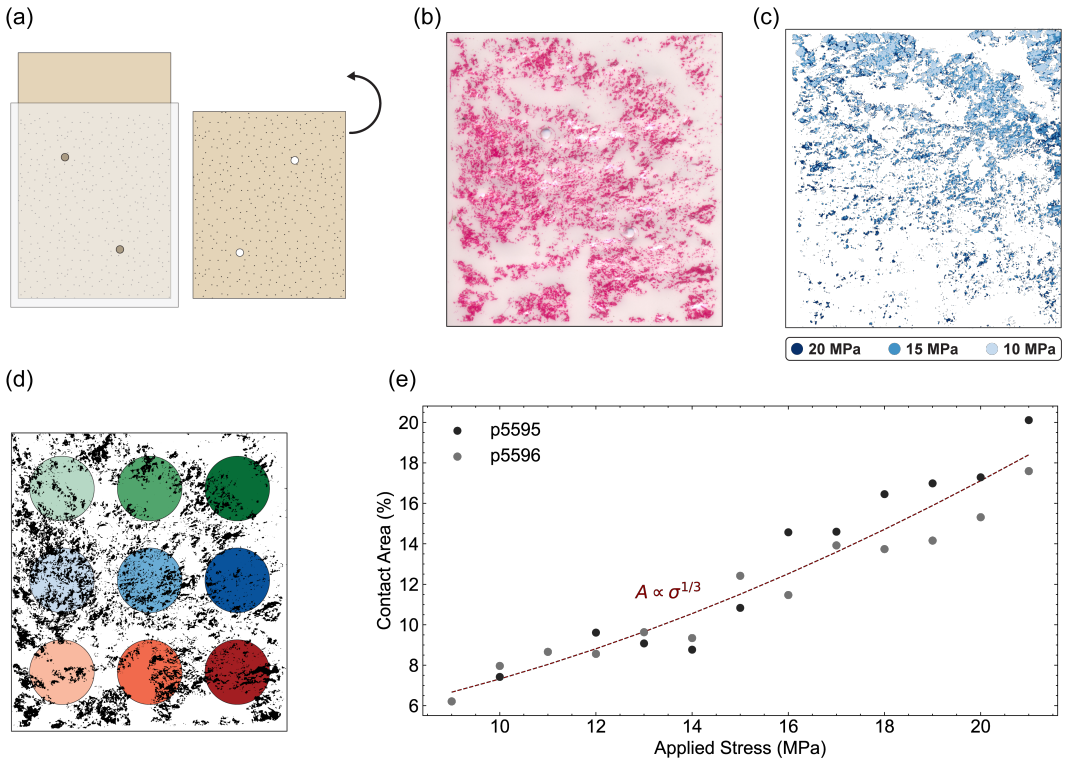

Figure 3. Integrating measurements of fracture contact area, aperture and elastic properties. (a) Sketch of fracture and locating pins to insert pressure sensitive film. (b) Example of pressure sensitive film after loading to 10 MPa (experiment p5596). Magenta regions represent contact and remaining areas are voids. (c) Superimposed images showing the evolution of contact area with applied stress at 10, 15, and 20 MPa. (d) Colored circles represent fracture regions probed by the array of transmitter-receiver pairs. The footprint size is recovered from the half-power bandwidth of the Fresnel zone. (e) Real contact area from film measurements (as in b) relative to nominal total area as a function of applied stress. The dashed line shows a cubic fit to these data, suggesting a Hertzian-contact relation between area and stress.

5 Results and Discussion

Our data include measurements of fracture permeability, p-wave velocity and amplitude as well as fracture contact area. The transducer array and pressure sensitive film provide information on the spatial variability of fracture properties and its evolution during dynamic stressing. We integrate that data with fluid flow measurements to develop a detailed understanding of fracture properties.

5.1 Connecting Sensor Footprint and Contact Area

A crucial component to this study is connecting fracture contacts to the active-source monitoring data. We estimate the real fracture contact area probed by each transmitter-receiver pair by superimposing the calculated PZT footprints (Section 3.1) onto the digitized and binarized pressure sensitive films. Figure 3d shows an example of fracture contacts (black indicates regions of contact and white indicates void) with locations and sizes of sensor footprints highlighted. This demonstrates the highly variable spatial distribution of contacts across the fracture. Additionally, the estimated total area of contact as

a function of applied stress is shown in Figure 3e. The dashed red line shows a cubic fit to these data, suggesting a Hertzian-contact relation between real contact area (from pressure sensitive films) and nominal applied stress (Hertz, 1881). Furthermore, we quantify the change in real contact area within PZT footprints with stress, see Figure 4. As expected, the contact area within each PZT footprint generally increases with stress with a few exceptions, possibly due to the inevitable variations in mating of the two fracture surfaces at each stress level. A comparison between the regions probed by sensors highlighted with dark green (top right) and light orange (bottom left) illustrate the disparity of contact area, especially for experiment p5596. The relation between these results and nonlinear elastodynamic measurements are detailed in discussion section.

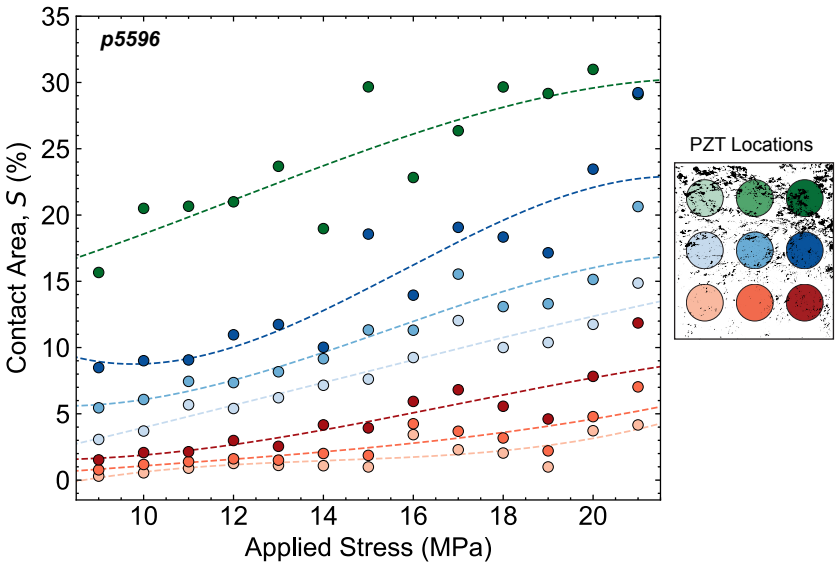

Figure 4. Percent area of fracture in contact within each PZT "footprint area" as a function of applied stress for one experiment. Contact area is directly estimated by pressure sensitive films at each stress. Note spatial variations in contact, as expected for a rough fracture, and also non-linear changes with stress. Each measurement involves re-mating the fracture and thus some variability is expected.

5.2 Hydraulic and Nonlinear Elastodynamic Responses

Rocks exhibit nonlinear elastic behavior due to the nonlinear response of their constituent minerals and structures, viz. microcracks and compliant grain boundaries (Guyer & Johnson, 2009; Rivière et al., 2015). When rocks are fractured, as in nature, this nonlinearity is compounded by contact acoustic nonlinearity at fractured interfaces. Figure 5 shows characteristic responses to dynamic pore fluid pressurization upstream (blue) where transient softening and modulation of baseline velocity (P. Johnson & Sutin, 2005) are manifest with slow recoveries to the pre-oscillation condition. In comparison, a linear elastic response would be effectively stress invariant, not showing any of the aforementioned characteristics. Thus, nonlinear elasticity reveals much about the rock microstructure, fractures, and inter-grain contacts (Guyer & Johnson, 2009), all of which also modulate the hydraulic properties. Both fluid and acoustic transmission characteristics are highly sensitive to pore/fracture apertures and contact condition. Thus, we seek to link the effect of stress state and resulting fracture aperture and contact to the elastodynamic and hydraulic properties of dynamically-stressed fractured rock. The nonlinear elastic response to dynamic stressing is characterized by the following: (1) relative

change in wave velocity, R_0, (2) the wave velocity amplitude modulation R_1, and (3) the evolution of slow dynamics or post-oscillation recovery of wave velocity c_r. Both R_0 and R_1 are extracted using a projection procedure following (Rivière et al., 2013). The long-term recovery, or slow dynamics, is observed to be logarithmic in time (Shokouhi et al., 2017b, 2017a; Ten Cate and Shankland, 1996) and is recorded in a 90 s window following each oscillation, although the time to full recovery may be much longer (Shokouhi et al., 2017a). Besides the nonlinear elastodynamic measures described above, the relative stress-induced change in permeability $\Delta k/k_0$ and log-time recovery k_r are quantified, as noted in the permeability subplot of Figure 5.

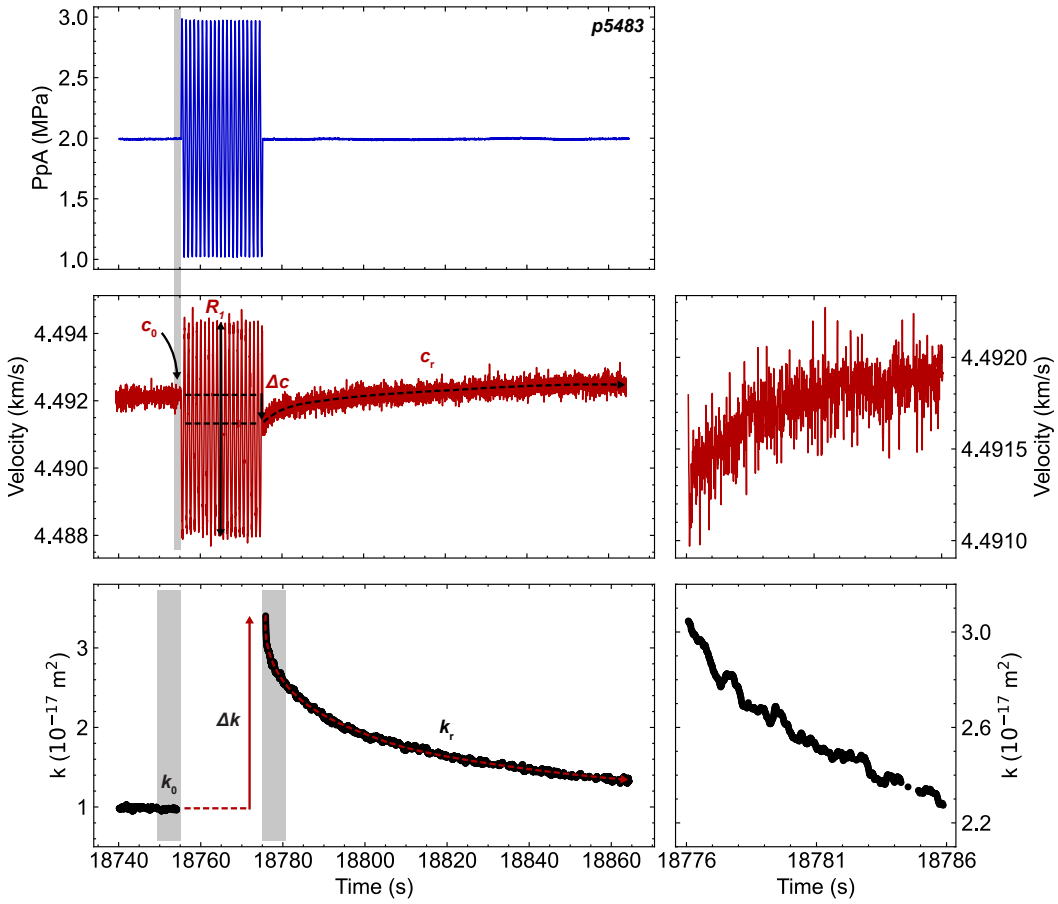

Figure 5. Excerpt of data from experiment p5483 illustrating the effect of pore pressure oscillation (1 MPa amplitude at 1 Hz) on ultrasonic p-wave velocity and permeability at applied normal stress of 20 MPa. A 1 second window preceding the oscillation is used to calculate the pre-oscillation values of velocity (c_0). Relative changes in velocity ($R_0 = \Delta c/c_0$) and wave velocity amplitude modulation (R_1) are extracted from the projection procedure. Changes in permeability are calculated from pre-oscillation, k_0, and post-oscillation magnitudes, k_1, averaged in 5 s windows, respectively. Long-term post-oscillation evolution in wave velocity and permeability (c_r, k_r respectively) are illustrated with arrows.

5.3 Dynamic Stress-induced Changes in Permeability

The relation between relative change in permeability ($\Delta k/k_0$) and pore pressure (P_{pA}) oscillation amplitude for each effective normal stress (σ_{eff}) ranging from 10 MPa

to 20 MPa in 2.5 MPa increments is shown in Figure 6a. All oscillations were applied with the same frequency of 1 Hz to allow direct comparison. As expected (Shokouhi et al., 2020; Wood et al., 2021), we observe increasing permeability enhancement with increasing amplitude of the applied pore pressure oscillation, though, in some cases this reaches a plateau. Additionally, the scaling between $\Delta k/k_0$ and oscillation amplitude (least-squares fit) varies with the stress state of the fracture, generally decreasing with increasing stress and assumed greater fracture closure, Figure 6b.

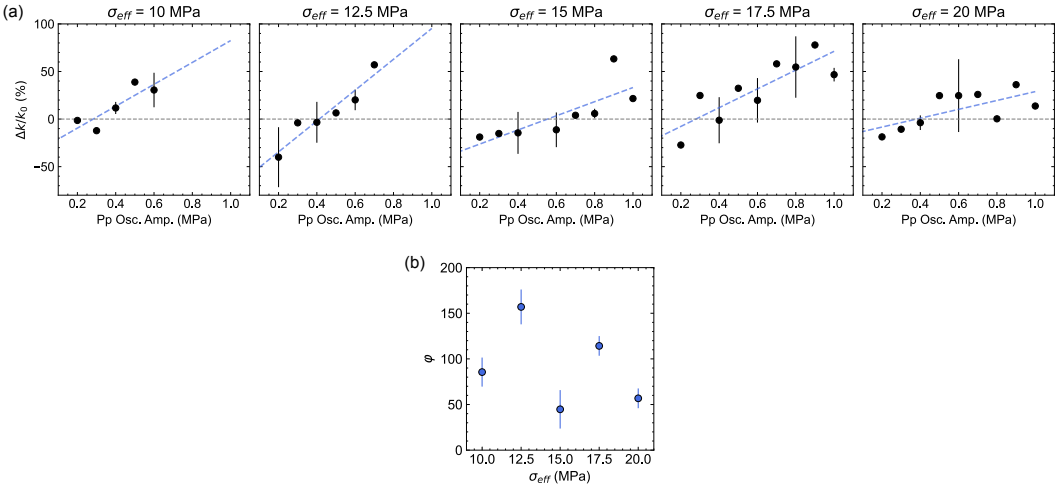

Figure 6. (a) Relative permeability change ($\Delta k/k_0$) as a function of pressure oscillation amplitude for each applied normal stress. For all applied normal stresses, permeability changes increase with increasing pressure oscillation amplitude. Error bars are one standard deviation from mean for oscillations with repetitions. (b) The ratio of change in relative permeability with pore pressure amplitude, φ, generally decreases with an increase in effective stress.

5.4 Dynamic Stress-induced Changes in P-wave Velocity

One of the measures of elastic nonlinearity, the relative change in velocity (R_0) for all transmitter-receiver pairs as a function of pore pressure oscillation amplitudes are shown in Figure 7a. As noted previously (Manogharan et al., 2021; Wood et al., 2021), the magnitude of R_0 clearly increases with increasing pressure oscillation amplitude. Furthermore, after an initial increase, increasing effective stress generally reduces the magnitude of R_0, as seen in Figure 7b in agreement with previous observations (Manogharan et al., 2021; Rivière et al., 2016). The data in Figure 7 are colored by location of the PZTs along the fracture plane (see scaled version in figure legend) to reveal the spatial variability of the measured nonlinearity.One observations across all stress levels is that the nonlinearity (larger magnitude R_0) measures the highest for the transducer pair at the bottom left corner (light pink color). In contrast, the nonlinearity measured by the transducer pair at the top right corner (dark green color) is among the lowest at all stress levels.

Another measure of elastodynamic nonlinearity that we investigate is the relative change in the average amplitude of the wave velocity change, R_1. Figure 8a shows R_1 as a function of pore pressure oscillation amplitude for all transmitter-receiver pairs. Like R_0, the average amplitude wave velocity R_1 scales linearly with increasing pore pressure oscillation amplitude, as expected (Rivière et al., 2015, 2013). As the fracture is closing with the increased applied stress, the slope of R_1 with respect to the oscillation am-

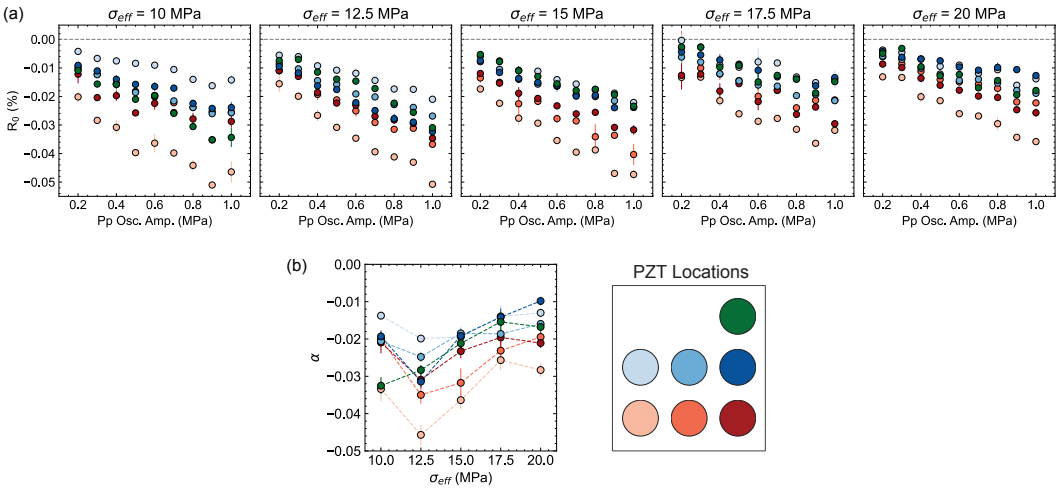

Figure 7. (a) Relative velocity change (R_0) averaged over repetitions at each oscillation amplitude as a function of amplitude. Symbol colors correspond to the highlighted transducer footprint locations (see legend). (b) Slope of R_0, α, versus oscillation amplitude for each normal stress, a measure of hysteretic nonlinearity. α decreases, then increases for most transmitter-receiver pairs. This represents a presumed fracture closure and increase in specific stiffness.

plitude denoted as β increases at 12.5 MPa, decreases, and then slightly increases again at 17.5 MPa, see Figure 8b. The trend is slightly different for different transducer pairs.

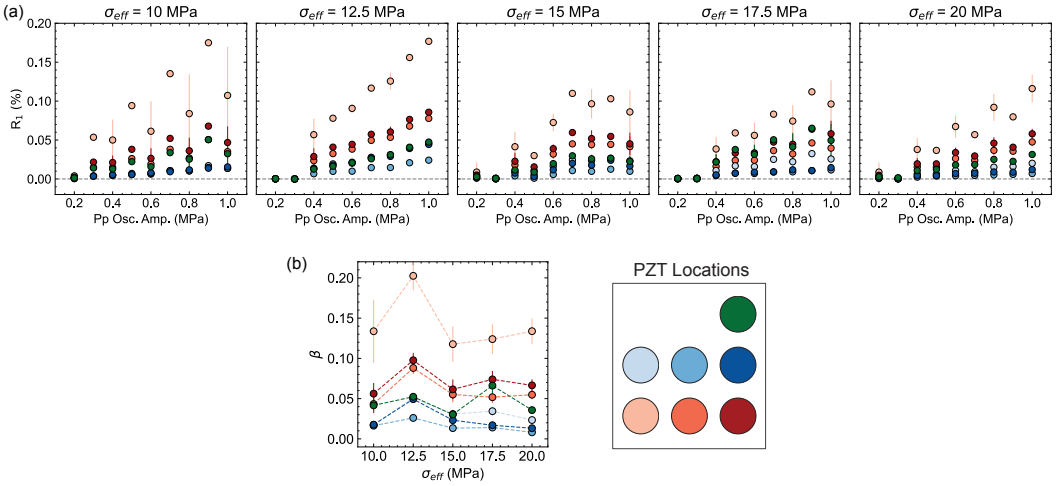

Figure 8. Relative change in the average amplitude of the wave velocity change (R_1) as a function of pressure oscillation amplitude. Symbol colors correspond to various ray path locations across the fracture. (b) Slope of R_1, β, versus pressure oscillation amplitude for increasing applied normal stress.

5.5 Linking Stress-Induced Elastodynamic and Hydraulic Changes

To investigate the coupling between fluid flow changes and elastodynamic nonlinearity, we analyze how the observed stress-induced changes in p-wave velocity is connected

to changes in permeability at different normal stress levels. Figure 9 relates stress-induced changes in p-wave velocity to changes in permeability ($\Delta k/k_0$) for each effective applied stress. In this figure, $\overline{R_0}$ denotes R_0 averaged over all transmitter-receiver pairs. Both of these parameters measure average changes along the fracture in response to stress perturbations. We observe a linear correlation between $\overline{R_0}$ and $\Delta k/k_0$, which appears to be mostly independent of the stress level. This is observed from the slope of the dashed red lines in Figure 9.

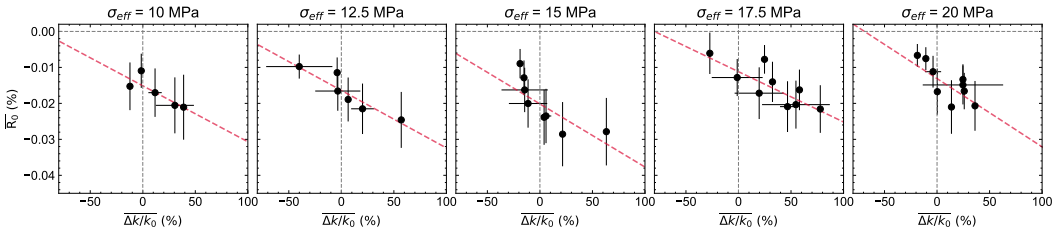

Figure 9. Relation between relative changes in velocity and permeability for each normal stress level.

5.6 Measurements during Loading vs. Unloading Phase

A key part of this study is understanding the effect of fracture aperture, degree to which fracture is closed or open under different applied stresses, on the stiffness and hydraulic properties of the fracture interface. Besides measurements at increasing effective stress levels (loading), we performed a subset of the pore pressure oscillation protocol while unloading the sample. During the unloading phase, the confining stress was decreased incrementally to the stresses previously used during the loading phase (17.5, 15, 12.5, 10) MPa. Figure 10 shows summarized results of the $\Delta k/k_0$ slope, φ, as a function of applied stress for both the loading (circle markers) and unloading (square markers) phases of experiment p5483. There is significant hysteresis comparing the loading phase to the unloading phase with nearly an order of magnitude difference between φ at the beginning and end of the loading cycle. During unloading, the values of φ only slightly increase. We posit that repeated stress oscillations and the large nominal stress $\sigma_{\text{eff}} = 20$ MPa cause permanent, plastic deformation of the fracture asperities, and as a result the preferred flow pathway(s) do not change significantly as the applied stress is reduced.

This hysteresis is also observed in the measures of nonlinearity, R_0 and R_1 albeit less pronounced. Figure 11 shows α measured for each transmitter-receiver pair as a function of applied stress for the loading and unloading phases of experiment p5483. During the loading phase, there is a characteristic decrease at $\sigma_{\text{eff}} = 12.5$ MPa (higher nonlinearity) and then an increase at $\sigma_{\text{eff}} = 20$ MPa (lower nonlinearity) for most of the transducer pairs. However, during the unloading phase, the change in α is either nearly invariant with applied stress (light blue, dark red) or linearly increases in magnitude. A common observation across all transducer pairs is the slightly higher measured nonlinearity during unloading than that during the loading phase at a given stress. Possibly, the asperities break and deform when loading leading to a larger instantaneous stress-induced stiffness change R_0 during unloading and therefore, larger α magnitudes. Similarly, Figure 12 shows β as a function of applied stress for each transmitter-receiver pair during the loading and unloading phases of the experiment. The measured β and hysteresis vary significantly for different transducers. The pairs in the two upper rows with β close to zero show nearly stress-invariant wave velocity amplitude modulation, whereas others in the bottom row show greater nonlinearity and hysteresis loops. As previously

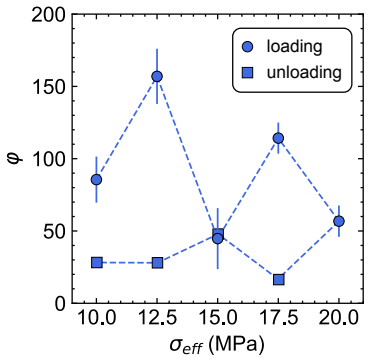

Figure 10. Slope of $\Delta k/k_0$, φ, as a function of applied stress for loading and unloading phases of the experiment. There is noticeable hysteresis during the unloading phase, where the lowest applied stress differs by an order of magnitude.

noted, the measured β during the loading phase is mostly insensitive to the effective stress level except for a local increase at 12.5 and a slight increase at 17.5 MPa for some transducer pairs. During the unloading phase, β generally increases returning to the initial value measured at 10 MPa. The observed hysteresis loops appear larger for transducer pairs with a larger measured β. Unlike what is observed for α, β measures consistently lower during unloading than loading. Previous studies relate β to opening and closing of fractures (Rivière et al., 2015). We hypothesize that the broken and deformed fracture asperities during loading facilitate the mating of the two fracture surfaces making it harder for the fracture and close thus smaller β. We note that for both α and β, the nonlinearity measured during unloading increases with decreasing stress, which is expected due to fracture opening.

5.7 Permeability Recovery and Slow Dynamics

The post-oscillation evolution of permeability and p-wave velocity is related to how the fracture contact asperities have been transiently or irreversibly changed during the imposed oscillations. Also, the time-dependent phenomenon provides an indication of the rate of healing and recovery at the perturbed interface. Here, this is measured as the slope of the recovery in logarithmic time. Our observations indicate that log-time permeability recovery k_r is mostly invariant to the amplitude of pore pressure oscillations at higher normal stresses ($>$ 12.5 MPa), Figure 13a. At lower normal stresses, the log-time evolution recovers more quickly at lower pore pressure oscillation amplitudes. These overall trends are summarized in Figure 13b with the slope of k_r as a function of applied stress, which also includes results from the unloading phase of the experiment.

The p-wave velocity recovery c_r for all transmitter-receiver pairs as a function of pore pressure oscillation amplitude is shown in Figure 14a. The measured recovery rate slightly increases with increasing pressure oscillation amplitude i.e., the wave velocity returns to the pre-oscillation value quicker after larger amplitude oscillations. The slopes change slightly and unsystematically with fracture closure, Figure 14b, but during the unloading phase, there is much less spread between the transmitter-receiver pairs and more systematic evolution with applied stress (fracture opening). In Figures 13b and 14b and 14c, both k_r and c_r slopes show a hysteretic relationship with fracture closing and opening (increasing and decreasing applied stress).

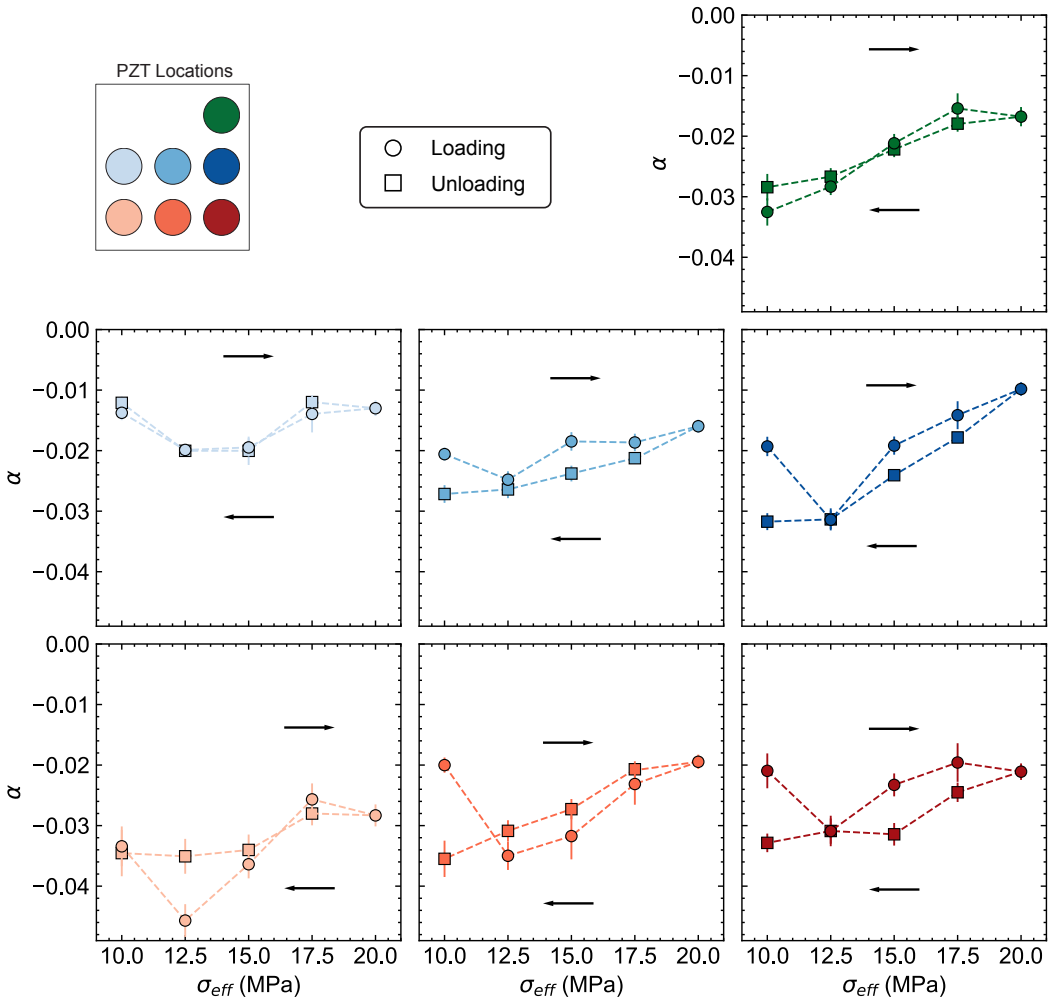

Figure 11. α vs. applied stress for loading and unloading phases of the experiment. A lower value of α corresponds to a larger nonlinearity. We see an overall decrease in nonlinearity with applied stress (α tends toward zero) for some of the pairs (e.g., dark green), while no clear trend can be seen for other pairs (i.e., light blue).

5.8 Relating Contact Area to Elastodynamic Properties

True fracture contact area constrain many of the elastodynamic and hydraulic observations. Figure 3c,e show that the estimated true contact area using pressure sensitive film increases as a function of applied stress in a Hertzian-contact-like manner (cubic relationship), effectively reducing aperture and enlarging individual contact areas. Defining Fresnel ray-path tunnels between transmitters and receivers (PZT footprints) projected on the pressure sensitive film images allows us to investigate the true contact area and its evolution for individual transducer pairs. Figure 4 confirms significant heterogeneity in the area of contact for various transmitter-receiver pairs at the same applied stress. We posit that this heterogeneous distribution in asperity contact resulting in spatial variation of specific stiffness across the fracture is a key factor behind the observed differences among nonlinear elastodynamic measurements from different transducer pairs.

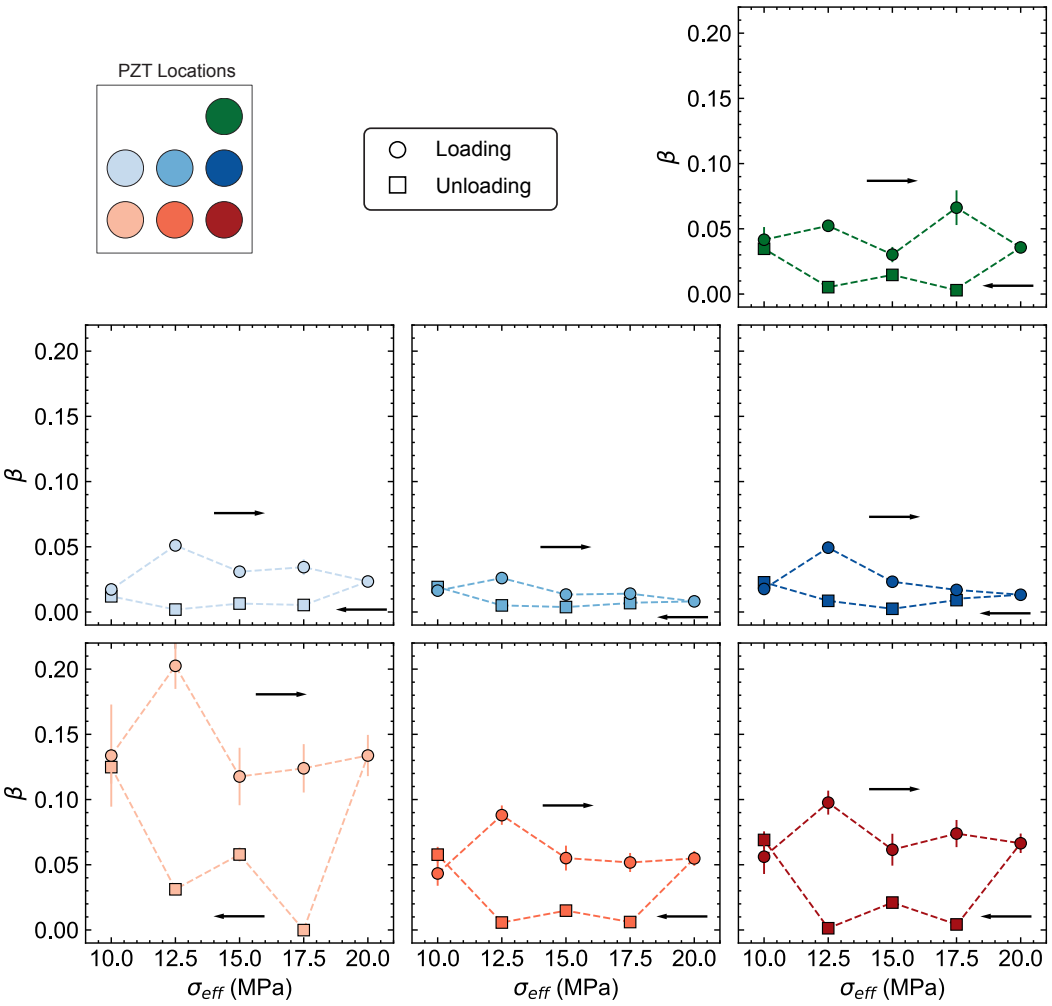

Figure 12. β vs. applied stress for loading and unloading phases of the experiment.

Next, we investigate the relationship between the nonlinear parameters and estimated contact area. Since stiffness is defined as $K = \frac{F}{S\delta}$, where δ is displacement, assuming a nominal unit area and considering the dependence of the contact force F on the number and radii of asperities in contact (Jin et al., 2020), we may take contact S_0 area to be a proxy for the interface stiffness at rest K_0. In other words, a fracture with a larger true contact area is expected to be stiffer. Similarly, the change in contact area due to dynamic stressing $\Delta S/S_0$ is expected to correlate with the change in stiffness $\Delta K/K_0$ and in turn with change in wave speed, the elastodynamic nonlinearity. Figure 15 shows the relative change in contact area ($\Delta S/S_0$) for each transmitter-receiver pair as a function of applied stress. S_0 is the contact area at each applied normal stress used in experiment p5483 ([10, 12.5, 15, 17.5, 20] MPa) and ΔS is the slope from a linear fit to the contact area ± 1 MPa at each stress level (for example, at 15 MPa, contact area obtained at 14, 15 and 16 MPa is used, see Figure 4). In the data from experiment p5596, most of the transmitter-receiver pairs follow a similar trend showing a modest increase in $\Delta S/S_0$ at 12 MPa, then a decrease at 17.5 MPa, followed by an increase at 20 MPa.

Since the nonlinearity parameter R_1 is believed to be related to the opening/closing of the fracture, it is considered to be a measure of $\Delta K/K_0$. Therefore, an important question to ask is whether our data show a correlation between R_1 and S_0 or $\Delta S/S_0$. To our

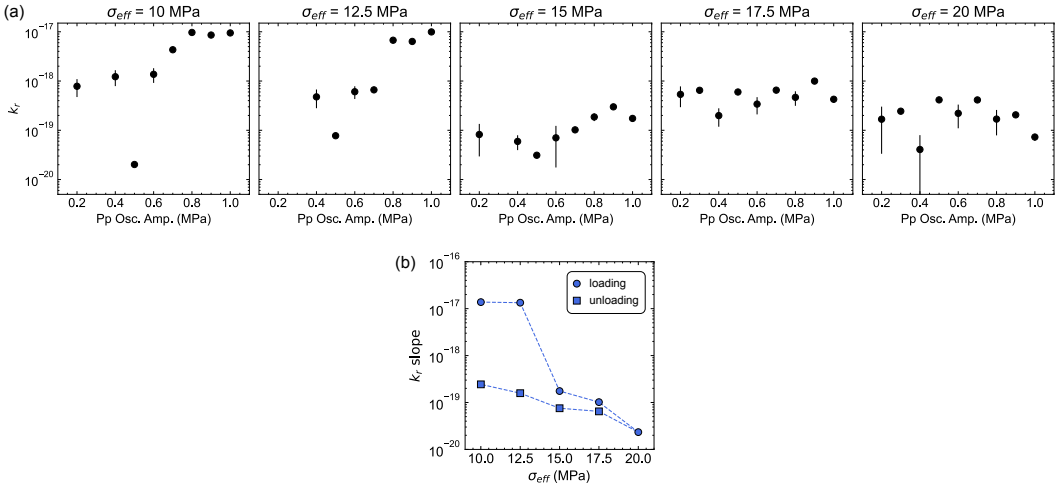

Figure 13. (a) Log-time recovery of permeability after pressure oscillations for each normal stress. The recovery rate is oscillation amplitude-dependent at lower stresses (< 15 MPa), but not at higher normal stresses (> 12.5 MPa) and with relatively little change up to the largest normal stress (20 MPa). (b) Slopes of k_r as a function of applied stress for the loading (black markers) and unloading (grey markers) phases of the experiment.

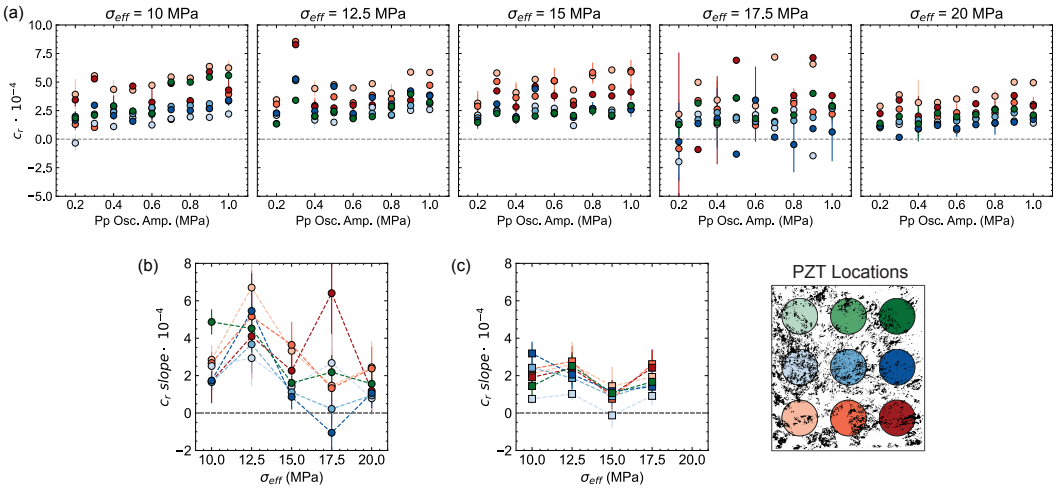

Figure 14. (a) Log-time recovery rate for all transmitter-receiver pairs. Positive values indicate a transient change to the fracture asperities and negative values indicate irreversible changes to fracture contacts. (b) The slope of c_r as a function of applied stress does not seem to systematically evolve with increasing σ_{eff}. (c) Slopes of c_r as a function of applied stress during the unloading phase of the experiment.

knowledge, this is the first experimental investigation of the relation between contact area and elastic nonlinearity of a fracture. The expectation is that regions of the fracture with a larger true contact area S_0 be stiffer and therefore, harder to open and close (at a given dynamic stress level); therefore, having a smaller S_0 is R_1 or β. This reasoning is supported by our observations shown in Figure 16. Following the same line of reasoning, one may expect a positive correlation between β and normalized change in area $\Delta S/S_0$. We attempt to investigate this relation in Figure 16, which shows $\Delta S/S_0$ as a function of

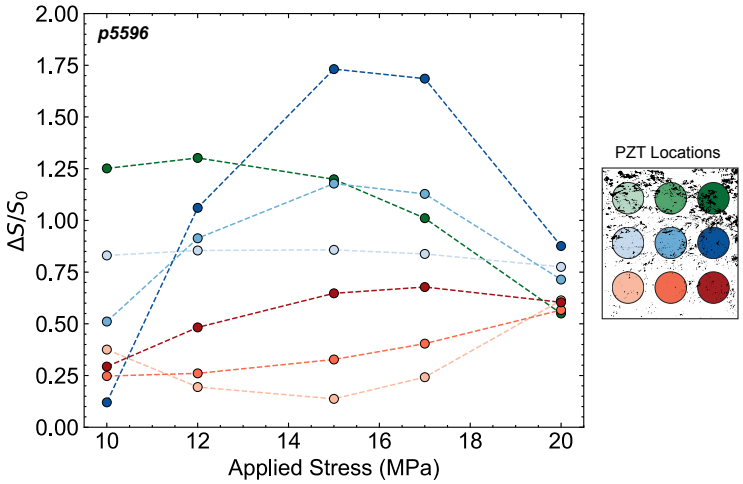

Figure 15. Relative change in contact area $\Delta S/S_0$ for each PZT pair as a function of applied stress for experiments p5595 and p5596. Most receivers (p5596) show a modest increase in $\Delta S/S_0$, then a decrease at 17.5 MPa, followed by an increase at 20 MPa.

β for all transmitter-receiver pairs, where we observe a negative correlation between the two quantities albeit with a lot of scatter. Figure 17 shows plot of $\Delta S/S_0$ *vs* S_0 reveals that the relative change in contact area generally increases with increasing contact area, which is counter-intuitive. This could be a result of errors in estimating ΔS, which relies on comparing the estimated contact areas at two different (but close) stress levels from two separate experiments.

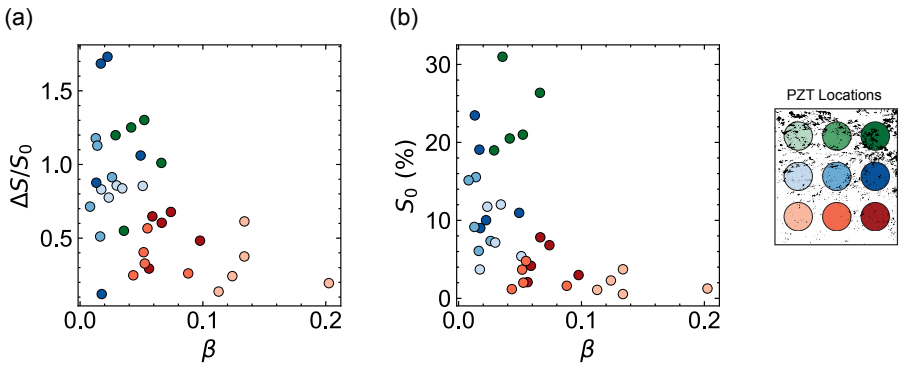

Figure 16. (a) Regions with larger contact area (S_0) exhibit smaller measure of nonlinearity, β, and regions with small S_0 exhibit larger nonlinearity. (b) Contact area change $\Delta S/S_0$ from experiment p5596 as a function of β for all transmitter-receiver pairs.

6 Conclusion

We present tightly-constrained experiments to investigate the role of aperture and real contact area on hydraulic and elastodynamic properties of dynamically-stressed fractured rock. Conditions are representative of fractures at various depths and therefore stresses. Simultaneous measurements of fluid flow and active-source ultrasonic transmis-

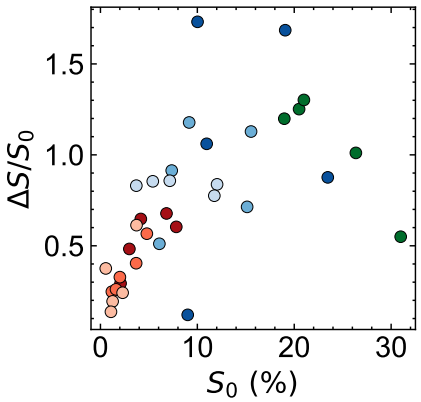

Figure 17. Comparison between contact area change $\Delta S/S_0$ and nominal contact area, S_0, for respective transmitter-receiver pairs. This reveals a counter-intuitive relation that the relative change in contact area generally increases with increasing contact area.

sion show how these mechanisms are coupled – potentially linking permeabilities with elastodynamic characteristics. Additionally, we quantify the heterogeneity of the fracture contacts at discrete stresses in order to better interpret our observations from multiple transducer pairs probing different parts of the fracture.

Fractured Westerly granite exhibits characteristic mesoscopic elastic nonlinearity when subjected to pore pressure oscillations, revealing rich information about the contact mechanics of the asperities. Our observations, as found in (Shokouhi et al., 2020; Wood et al., 2021), show a nearly monotonic relationship between increased permeability enhancement and increased pressure oscillation amplitude. We add to the work of (Shokouhi et al., 2020; Manogharan et al., 2021; Wood et al., 2021) by documenting a reduction in pore pressure oscillation-induced permeability enhancement with increasing normal stress on the fracture and related fracture closure. Similar trends are observed for the nonlinearity parameters α and β. For some transmitter-receiver pairs, the nonlinearity parameters depend on the degree of fracture openness (in the corresponding region of the fracture) immediately before oscillation. There is a noticeable increase in nonlinearity, α and β, from 10 MPa to 12.5 MPa, for example (see Figures 7b and 8b). That is to say, the dominating factor is not necessarily the stress state, but the local fracture aperture.

We investigate the spatial heterogeneity of nonlinearity parameters with regard to actual estimations of fracture contacts and voids. To that end, pressure sensitive film images are related to ultrasonic measurements; a smaller initial contact area (S_0) is associated with higher nonlinearity β and a larger S_0 with a smaller β . To our knowledge, this is the first experimental results relating fracture true contact area and elastodynamic nonlinearity. Although the evolution of contact asperities ($\Delta S/S_0$) proved to be difficult to measure, our results, though scattered, suggest that, smaller changes in contact area are correlated with a higher degree of nonlinearity and vice versa, see Figure 16.

Finally, we document the rate of recovery from post-oscillation state of permeability and wave velocity. The rate of permeability recovery (log-time) increases above $\sim 0.4 - 0.6$ MPa amplitude oscillations at lower stresses ($\sigma_{\text{eff}} < 17.5$MPa) and oscillation amplitude-invariant at higher stresses ($\sigma_{\text{eff}} > 15$MPa), (see Figure 13). These recovery rates are orders of magnitude smaller than those reported in previous studies (Shokouhi et al., 2020; Wood et al., 2021), where gouge present at the fracture interface dominated permeability changes. During the unloading phase, the rate of recovery increases with

decreasing stress state. These recovery rates are also smaller than in previous studies (Shokouhi et al., 2020; Wood et al., 2021), suggesting "accumulated deformation" throughout the loading phase of the experiment.

Data Availability Statement

Data for hydraulic, mechanical, and ultrasonic (time delay) for this research are available at https://doi.org/10.5281/zenodo.7392037.

Acknowledgments

Technical assistance from Steven Swavely is gratefully acknowledged. This work was fully supported by a grant from DOE Office of Basic Energy Science (DE-SC0017585) to PS. CM acknowledges support from the European Research Council Advance Grant 835012 (TECTONIC) and US Department of Energy grants DE-SC0020512 and DE-EE0008763.

References

Boettcher, M., & Marone, C. (2004). Effects of normal stress variation on the strength and stability of creeping faults. *Journal of Geophysical Research: Solid Earth*, *109*(B3).

Brenguier, F., Campillo, M., Hadziioannou, C., Shapiro, N. M., Nadeau, R. M., & Larose, E. (2008). Postseismic relaxation along the san andreas fault at parkfield from continuous seismological observations. *Science*, *321*(5895), 1478–1481. Retrieved from `https://science.sciencemag.org/content/321/5895/1478` doi: 10.1126/science.1160943

Brodsky, E. E., & Lajoie, L. J. (2013). Anthropogenic seismicity rates and operational parameters at the salton sea geothermal field. *Science*, *341*(6145), 543-546. Retrieved from `https://www.science.org/doi/abs/10.1126/science.1239213` doi: 10.1126/science.1239213

Candela, T., Brodsky, E. E., Marone, C., & Elsworth, D. (2014). Laboratory evidence for particle mobilization as a mechanism for permeability enhancement via dynamic stressing. *Earth and Planetary Science Letters*, *392*, 279-291. doi: https://doi.org/10.1016/j.epsl.2014.02.025

Candela, T., Brodsky, E. E., Marone, C., & Elsworth, D. (2015). Flow rate dictates permeability enhancement during fluid pressure oscillations in laboratory experiments. *Journal of Geophysical Research: Solid Earth*, *120*(4), 2037-2055. Retrieved from `https://agupubs.onlinelibrary.wiley.com/doi/abs/10.1002/2014JB011511` doi: https://doi.org/10.1002/2014JB011511

Elkhoury, J. E., Niemeijer, A., Brodsky, E. E., & Marone, C. (2011). Laboratory observations of permeability enhancement by fluid pressure oscillation of in situ fractured rock. *Journal of Geophysical Research: Solid Earth*, *116*(B2). Retrieved from `https://agupubs.onlinelibrary.wiley.com/doi/abs/10.1029/2010JB007759` doi: https://doi.org/10.1029/2010JB007759

Guyer, R. A., & Johnson, P. A. (2009). *Nonlinear mesoscopic elasticity: the complex behaviour of rocks, soil, concrete*. John Wiley & Sons.

Healy, J. H., Rubey, W. W., Griggs, D. T., & Raleigh, C. B. (1968). The denver earthquakes. *Science*, *161*(3848), 1301–1310. Retrieved from `https://science.sciencemag.org/content/161/3848/1301` doi: 10.1126/science.161.3848.1301

Hedayat, A., Pyrak-Nolte, L. J., & Bobet, A. (2014, August). Precursors to the shear failure of rock discontinuities: Precursors to Rock Frictional Sliding. *Geophys. Res. Lett.*, *41*(15), 5467–5475. Retrieved 2022-02-07, from `http://doi.wiley.com/10.1002/2014GL060848` doi: 10.1002/2014GL060848

Hertz, H. (1881). On the contact of elastic solids. *Z. Reine Angew. Mathematik*, *92*, 156–171.

Ishibashi, T., Elsworth, D., Fang, Y., Rivière, J., Madara, B., Asanuma, H., ... Marone, C. (2018). Friction-stability-permeability evolution of a fracture in granite. *Water Resources Research*, *54*(12), 9901-9918. Retrieved from https://agupubs.onlinelibrary.wiley.com/doi/abs/10.1029/2018WR022598 doi: https://doi.org/10.1029/2018WR022598

Jin, J., Johnson, P., & Shokouhi, P. (2020). An integrated analytical and experimental study of contact acoustic nonlinearity at rough interfaces of fatigue cracks. *Journal of the Mechanics and Physics of Solids*, *135*, 103769.

Johnson, P., & Sutin, A. (2005). Slow dynamics and anomalous nonlinear fast dynamics in diverse solids. *The Journal of the Acoustical Society of America*, *117*(1), 124-130. Retrieved from https://doi.org/10.1121/1.1823351 doi: 10.1121/1.1823351

Johnson, P. A., Carmeliet, J., Savage, H. M., Scuderi, M., Carpenter, B. M., Guyer, R. A., ... Marone, C. (2016). Dynamically triggered slip leading to sustained fault gouge weakening under laboratory shear conditions. *Geophysical Research Letters*, *43*(4), 1559-1565. Retrieved from https://agupubs.onlinelibrary.wiley.com/doi/abs/10.1002/2015GL067056 doi: https://doi.org/10.1002/2015GL067056

Liu, W., & Manga, M. (2009). Changes in permeability caused by dynamic stresses in fractured sandstone. *Geophysical Research Letters*, *36*(20).

Manogharan, P., Wood, C., Marone, C., Elsworth, D., Rivière, J., & Shokouhi, P. (2021). Nonlinear elastodynamic behavior of intact and fractured rock under in-situ stress and saturation conditions. *Journal of the Mechanics and Physics of Solids*, *153*, 104491. Retrieved from https://www.sciencedirect.com/science/article/pii/S0022509621001605 doi: https://doi.org/10.1016/j.jmps.2021.104491

McGarr, A., Bekins, B., Burkardt, N., Dewey, J., Earle, P., Ellsworth, W., ... Sheehan, A. (2015). Coping with earthquakes induced by fluid injection. *Science*, *347*(6224), 830–831. Retrieved from https://science.sciencemag.org/content/347/6224/830 doi: 10.1126/science.aaa0494

McNamara, D. E., Hayes, G. P., Benz, H. M., Williams, R. A., McMahon, N. D., Aster, R. C., ... Earle, P. (2015). Reactivated faulting near cushing, oklahoma: Increased potential for a triggered earthquake in an area of united states strategic infrastructure. *Geophysical Research Letters*, *42*(20), 8328-8332. Retrieved from https://agupubs.onlinelibrary.wiley.com/doi/abs/10.1002/2015GL064669 doi: https://doi.org/10.1002/2015GL064669

Raleigh, C. B., Healy, J. H., & Bredehoeft, J. D. (1976). An experiment in earthquake control at rangely, colorado. *Science*, *191*(4233), 1230–1237. Retrieved from https://science.sciencemag.org/content/191/4233/1230 doi: 10.1126/science.191.4233.1230

Rivière, J., Renaud, G., Guyer, R. A., & Johnson, P. A. (2013). Pump and probe waves in dynamic acousto-elasticity: Comprehensive description and comparison with nonlinear elastic theories. *Journal of Applied Physics*, *114*(5), 054905. Retrieved from https://doi.org/10.1063/1.4816395 doi: 10.1063/1.4816395

Rivière, J., Shokouhi, P., Guyer, R. A., & Johnson, P. A. (2015). A set of measures for the systematic classification of the nonlinear elastic behavior of disparate rocks. *Journal of Geophysical Research: Solid Earth*, *120*(3), 1587-1604. Retrieved from https://agupubs.onlinelibrary.wiley.com/doi/abs/10.1002/2014JB011718 doi: https://doi.org/10.1002/2014JB011718

Rivière, J., Pimienta, L., Scuderi, M., Candela, T., Shokouhi, P., Fortin, J., ... Johnson, P. A. (2016). Frequency, pressure, and strain dependence of nonlinear elasticity in berea sandstone. *Geophysical Research Letters*, *43*(7), 3226-

3236. Retrieved from https://agupubs.onlinelibrary.wiley.com/doi/abs/10.1002/2016GL068061 doi: https://doi.org/10.1002/2016GL068061

Roberts, P. M. (2005). Laboratory observations of altered porous fluid flow behavior in berea sandstone induced by low-frequency dynamic stress stimulation. *Acoustical Physics*, *51*, S140-S148.

Roberts, P. M., & Abdel-Fattah, A. I. (2009). Seismic stress stimulation mobilizes colloids trapped in a porous rock. *Earth and Planetary Science Letters*, *284*(3-4), 538–543.

Roux, P., Marandet, C., Nicolas, B., & Kuperman, W. A. (2013, July). Experimental measurement of the acoustic sensitivity kernel. *The Journal of the Acoustical Society of America*, *134*(1), EL38–EL44. Retrieved 2022-02-09, from http://asa.scitation.org/doi/10.1121/1.4808111 doi: 10.1121/1.4808111

Savage, H. M., & Marone, C. (2007). Effects of shear velocity oscillations on stick-slip behavior in laboratory experiments. *Journal of Geophysical Research: Solid Earth*, *112*(B2).

Shokouhi, P., Jin, J., Wood, C., Rivière, J., Madara, B., Elsworth, D., & Marone, C. (2020). Dynamic stressing of naturally fractured rocks: On the relation between transient changes in permeability and elastic wave velocity. *Geophysical Research Letters*, *47*(1), e2019GL083557. Retrieved from https://agupubs.onlinelibrary.wiley.com/doi/abs/10.1029/2019GL083557 (e2019GL083557 2019GL083557) doi: https://doi.org/10.1029/2019GL083557

Shokouhi, P., Rivière, J., Guyer, R. A., & Johnson, P. A. (2017). Slow dynamics of consolidated granular systems: Multi-scale relaxation. *Applied Physics Letters*, *111*(25), 251604. Retrieved from https://doi.org/10.1063/1.5010043 doi: 10.1063/1.5010043

Shreedharan, S., Bolton, D. C., Rivière, J., & Marone, C. (2021, January). Competition between preslip and deviatoric stress modulates precursors for laboratory earthquakes. *Earth and Planetary Science Letters*, *553*, 116623. Retrieved 2022-02-07, from https://linkinghub.elsevier.com/retrieve/pii/S0012821X20305677 doi: 10.1016/j.epsl.2020.116623

Simpson, D., Leith, W., & Scholz, C. (1988, 12). Two types of reservoir-induced seismicity. *Bulletin of the Seismological Society of America*, *78*(6), 2025-2040.

Sminchak, J., & Gupta, N. (2003, 06). Aspects of induced seismic activity and deep-well sequestration of carbon dioxide. *Environmental Geosciences*, *10*(2), 81-89. Retrieved from https://doi.org/10.1306/eg.04040302009 doi: 10.1306/eg.04040302009

Spetzler, J., & Snieder, R. (2004, May). The Fresnel volume and transmitted waves. *GEOPHYSICS*, *69*(3), 653–663. Retrieved 2022-02-09, from https://library.seg.org/doi/10.1190/1.1759451 doi: 10.1190/1.1759451

van der Elst, N. J., Savage, H. M., Keranen, K. M., & Abers, G. A. (2013). Enhanced remote earthquake triggering at fluid-injection sites in the mid-western united states. *Science*, *341*(6142), 164-167. Retrieved from https://www.science.org/doi/abs/10.1126/science.1238948 doi: 10.1126/science.1238948

Walsh, F. R., & Zoback, M. D. (2015). Oklahoma's recent earthquakes and saltwater disposal. *Science Advances*, *1*(5). Retrieved from https://advances.sciencemag.org/content/1/5/e1500195 doi: 10.1126/sciadv.1500195

Wood, C., Shokouhi, P., Manogharan, P., Rivère, J., Elsworth, D., & Marone, C. (2021). Imaging elastodynamic and hydraulic properties of in situ fractured rock: An experimental investigation exploring effects of dynamic stressing and shearing. *Journal of Geophysical Research: Solid Earth*, *126*(11), e2020JB021521. Retrieved from https://agupubs.onlinelibrary.wiley.com/doi/abs/10.1029/2020JB021521 (e2020JB021521 2020JB021521) doi: https://doi.org/10.1029/2020JB021521

Zhang, F., Fang, Y., Elsworth, D., Wang, C., & Yang, X. (2017). Evolution of Friction and Permeability in a Propped Fracture under Shear. *Geofluids*, *2017*, 2063747. Retrieved from https://doi.org/10.1155/2017/2063747 doi: 10.1155/2017/2063747

Zhang, Y., Nishizawa, O., Kiyama, T., & Xue, Z. (2015, July). Saturation-path dependency of P-wave velocity and attenuation in sandstone saturated with CO_2 and brine revealed by simultaneous measurements of waveforms and X-ray computed tomography images. *GEOPHYSICS*, *80*(4), D403–D415. Retrieved 2022-02-09, from https://library.seg.org/doi/10.1190/geo2014-0289.1 doi: 10.1190/geo2014-0289.1

Figure1.

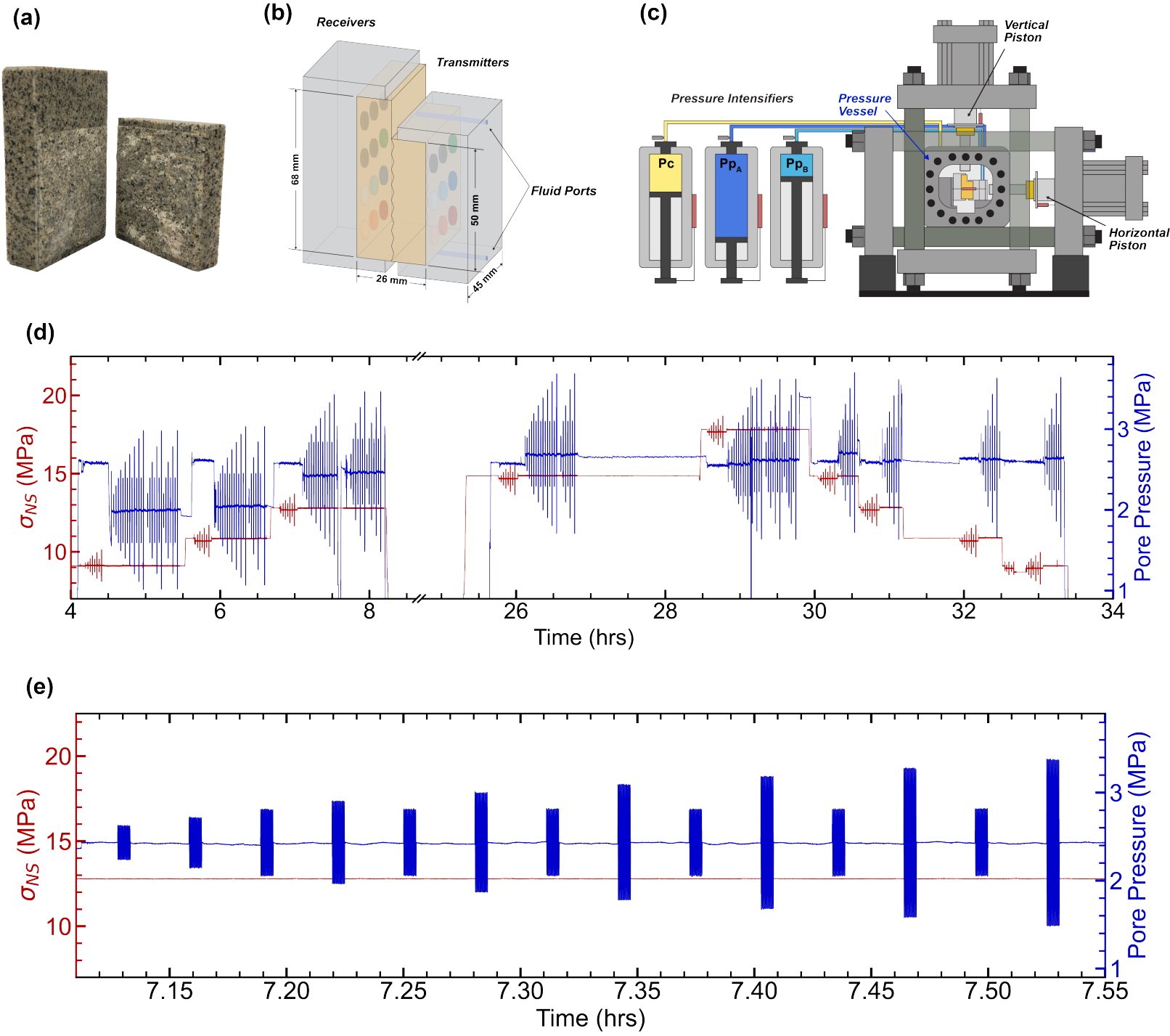
(a)
(b)
Receivers
Transmitters
68 mm
50 mm
26 mm
45 mm
Fluid Ports
(c)
Vertical Piston
Pressure Intensifiers
Pressure Vessel
Pc
PpA
PpB
Horizontal Piston
(d)
σNS (MPa)
Pore Pressure (MPa)
Time (hrs)
(e)
σNS (MPa)
Pore Pressure (MPa)
Time (hrs)

Figure2.

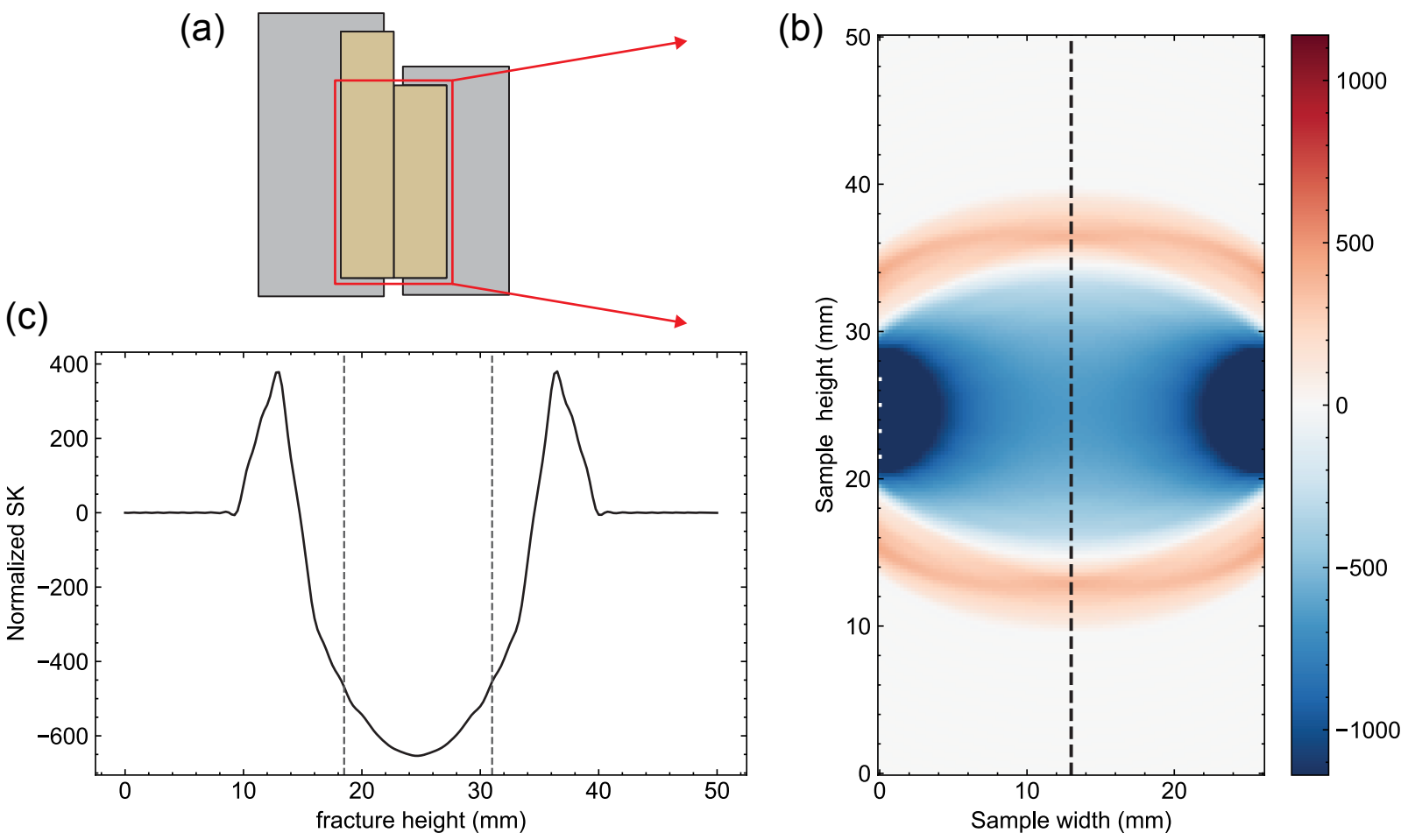
(a)
(b)
(c)
Normalized SK
fracture height (mm)
Sample height (mm)
Sample width (mm)
400
200
0
−200
−400
−600
50
40
30
20
10
0
1000
500
0
−500
−1000

Figure3.

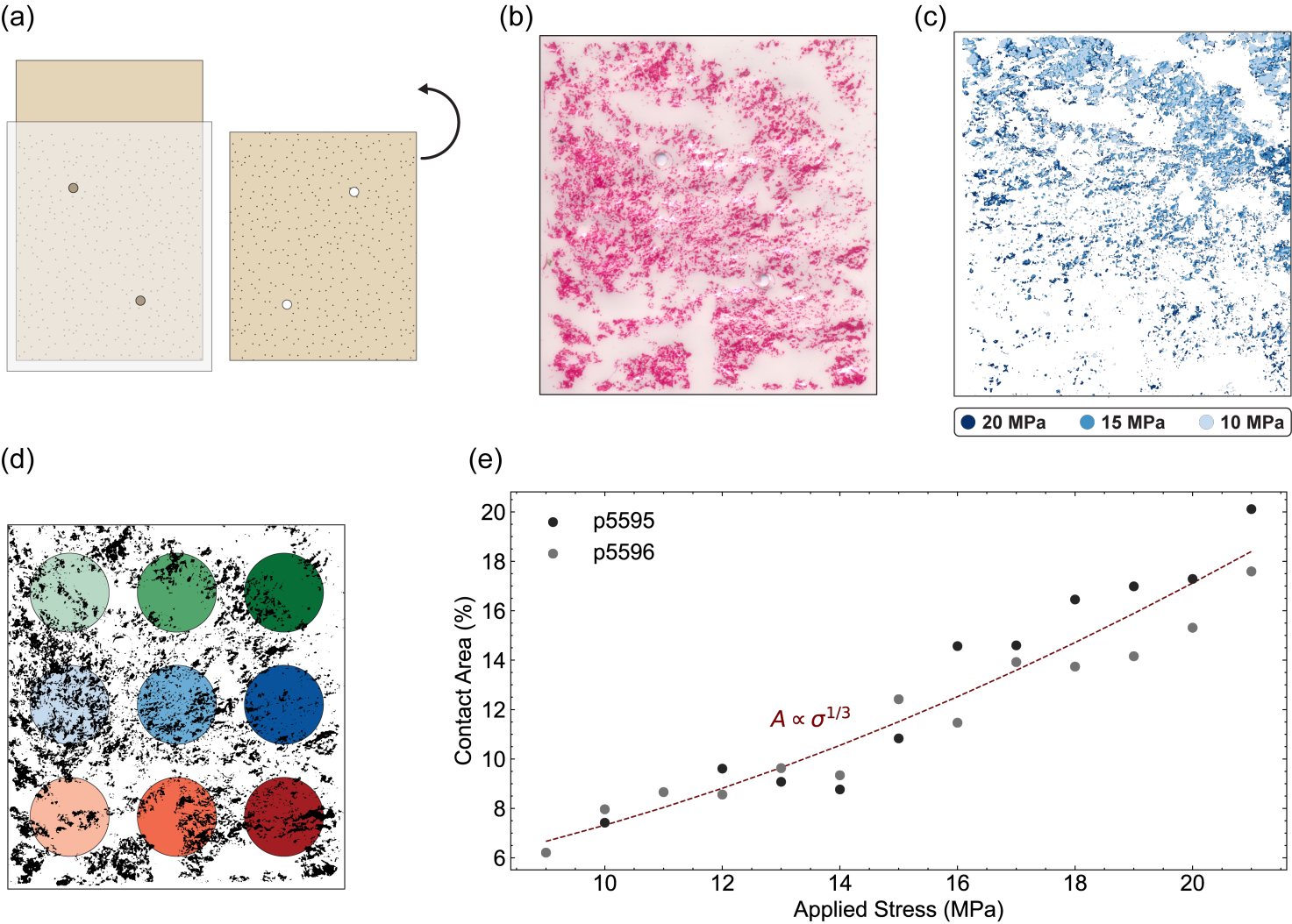
(a)
(b)
(c)
20 MPa
15 MPa
10 MPa
(d)
(e)
p5595
p5596
$A \propto \sigma^{1/3}$
Contact Area (%)
Applied Stress (MPa)
6
8
10
12
14
16
18
20
10
12
14
16
18
20

Figure4.

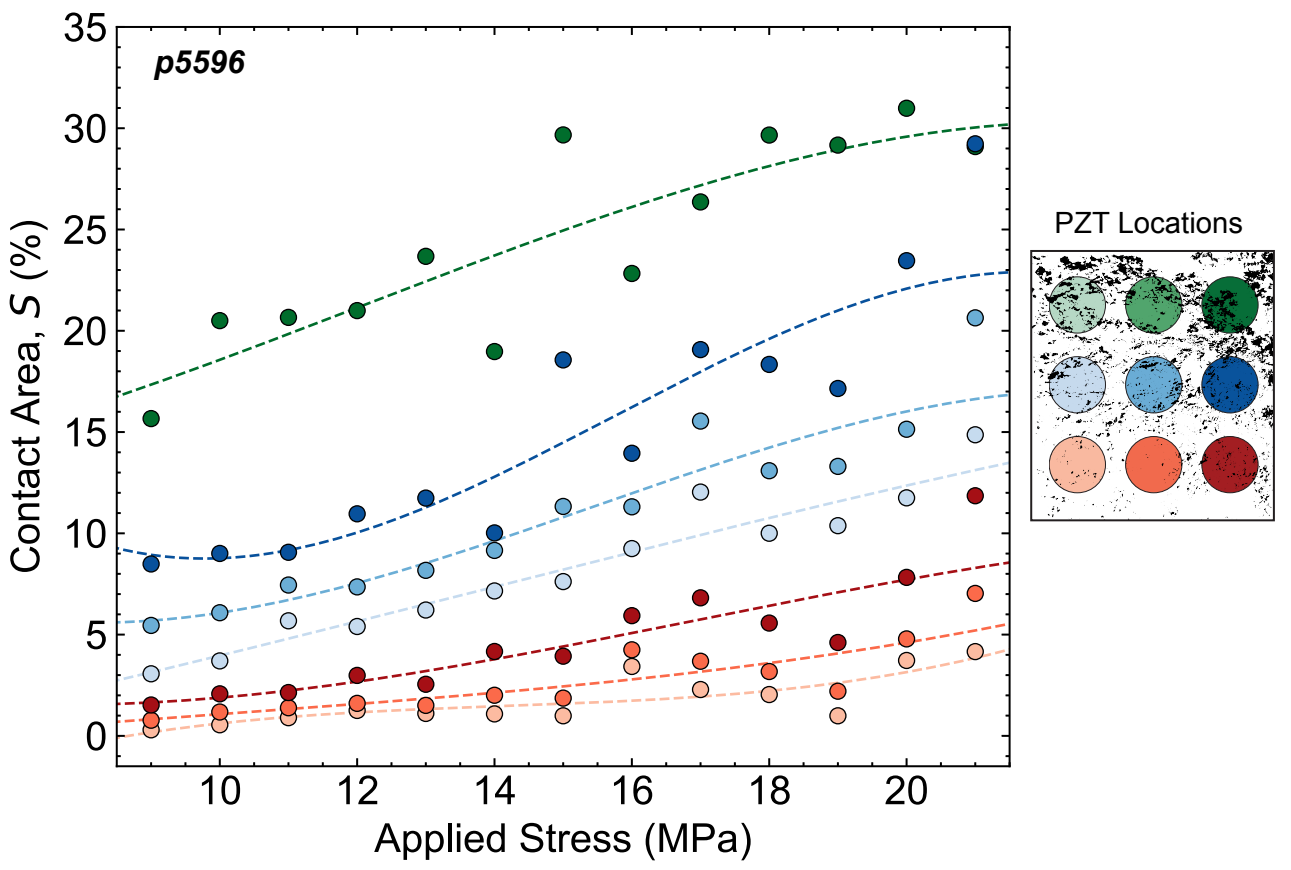
p5596
Contact Area, S (%)
Applied Stress (MPa)
PZT Locations

Figure5.

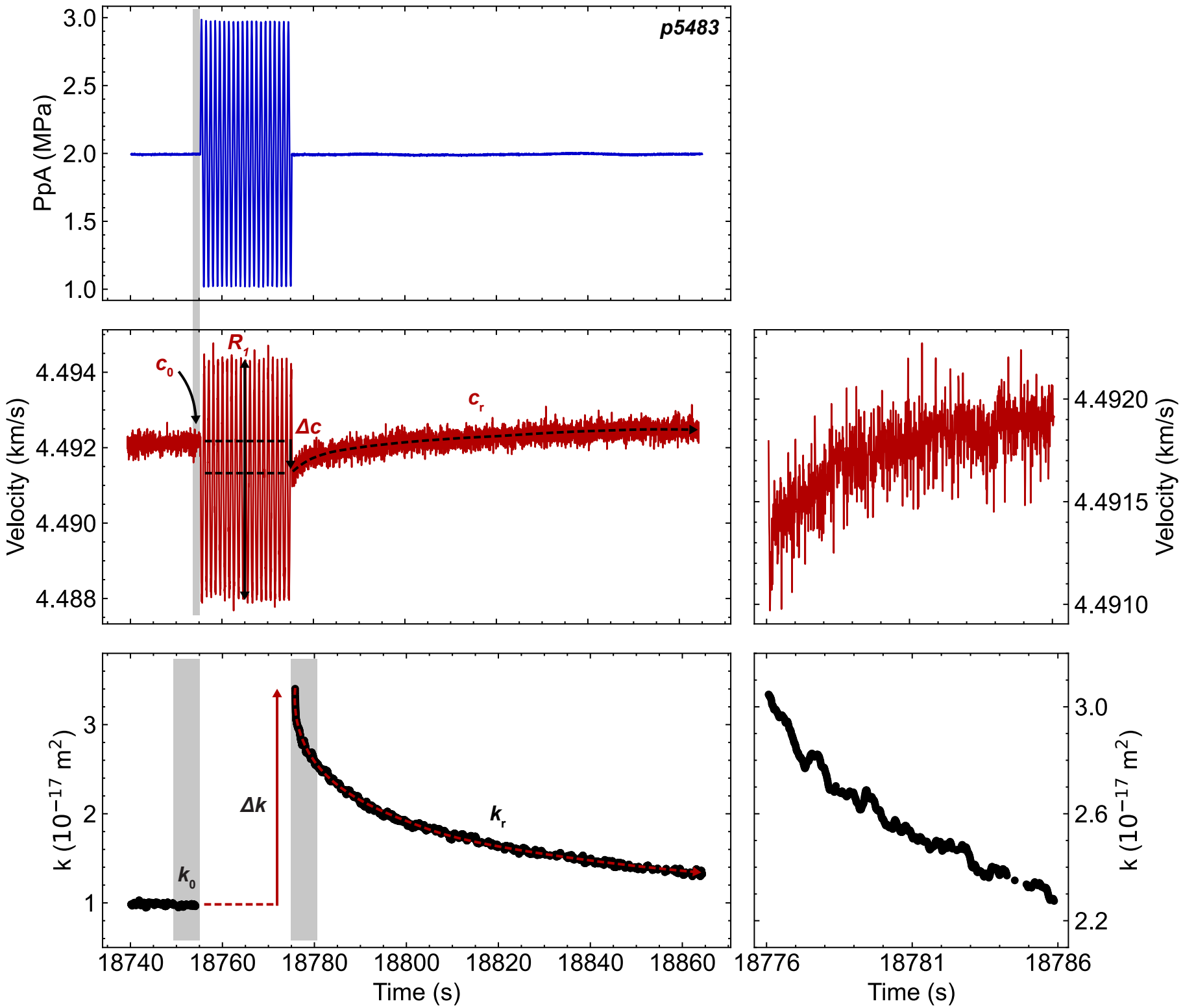
p5483
PpA (MPa)
3.0
2.5
2.0
1.5
1.0
Velocity (km/s)
4.494
4.492
4.490
4.488
c_0
R_1
Δc
c_r
4.4920
4.4915
4.4910
Velocity (km/s)
k (10^{-17} m^2)
3
2
1
Δk
k_0
k_r
3.0
2.6
2.2
k (10^{-17} m^2)
18740
18760
18780
18800
18820
18840
18860
Time (s)
18776
18781
18786
Time (s)

Figure6.

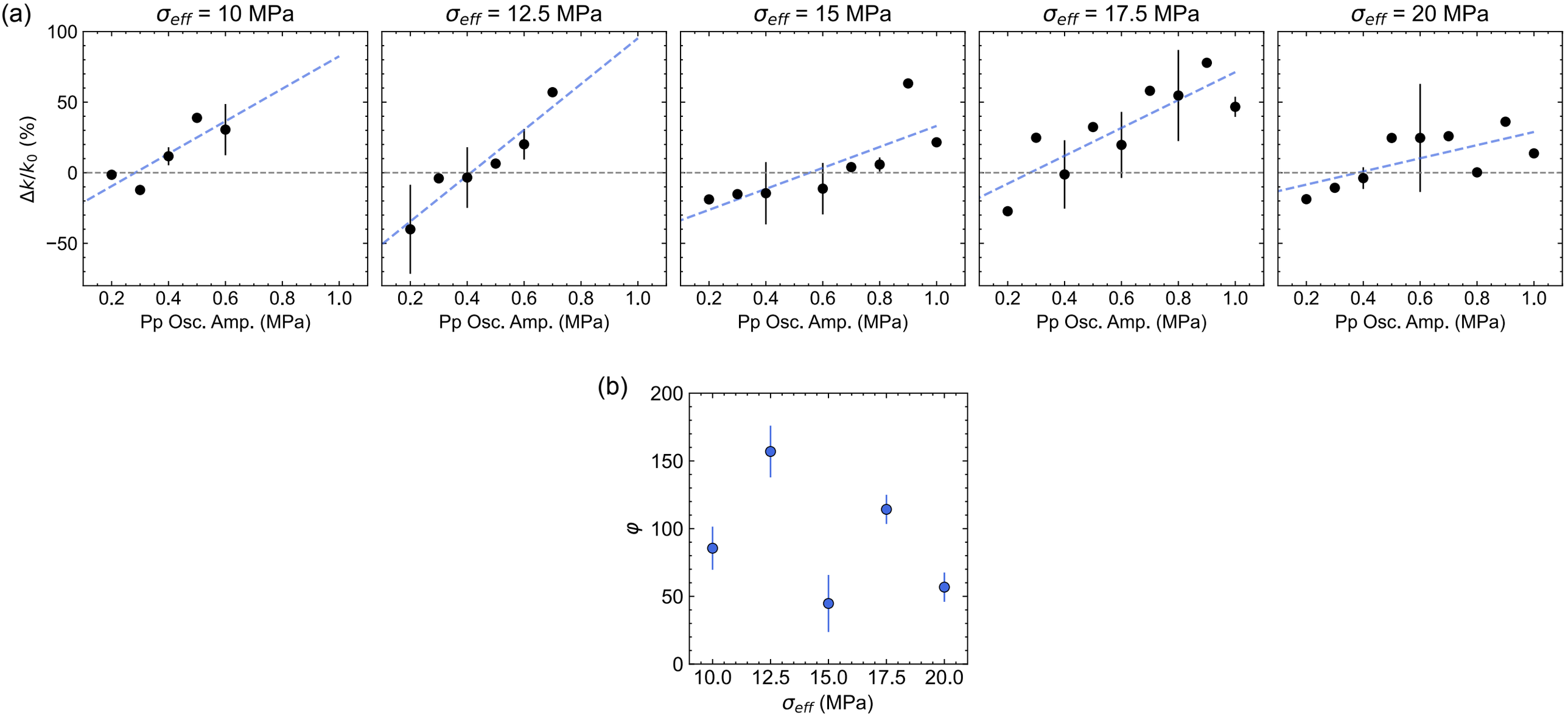
(a)
σ_{eff} = 10 MPa
σ_{eff} = 12.5 MPa
σ_{eff} = 15 MPa
σ_{eff} = 17.5 MPa
σ_{eff} = 20 MPa
$\Delta k/k_0$ (%)
100
50
0
−50
0.2
0.4
0.6
0.8
1.0
Pp Osc. Amp. (MPa)
(b)
φ
200
150
100
50
0
10.0
12.5
15.0
17.5
20.0
σ_{eff} (MPa)

Figure7.

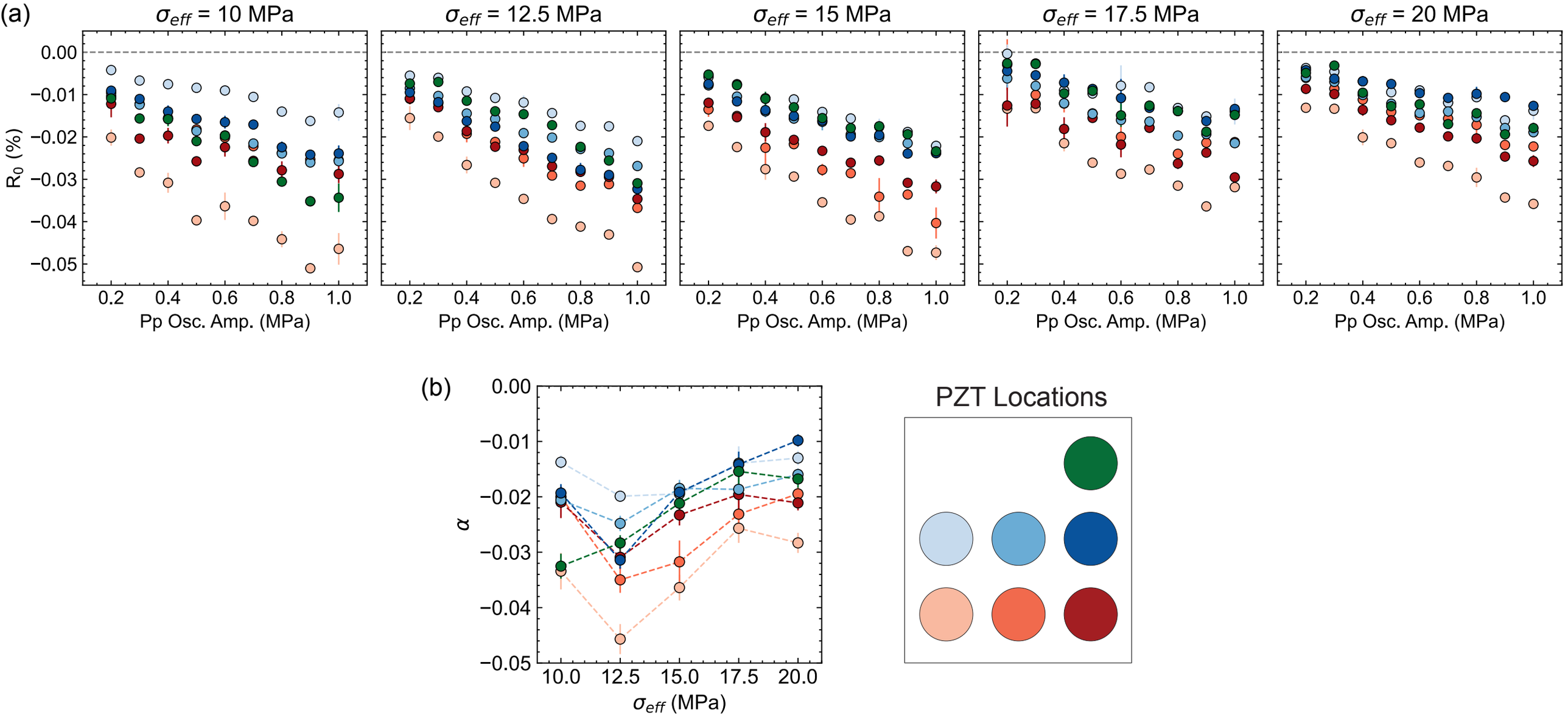
(a)
σ_{eff} = 10 MPa
σ_{eff} = 12.5 MPa
σ_{eff} = 15 MPa
σ_{eff} = 17.5 MPa
σ_{eff} = 20 MPa
R_0 (%)
0.00
−0.01
−0.02
−0.03
−0.04
−0.05
0.2
0.4
0.6
0.8
1.0
Pp Osc. Amp. (MPa)
(b)
α
10.0
12.5
15.0
17.5
20.0
σ_{eff} (MPa)
PZT Locations

Figure8.

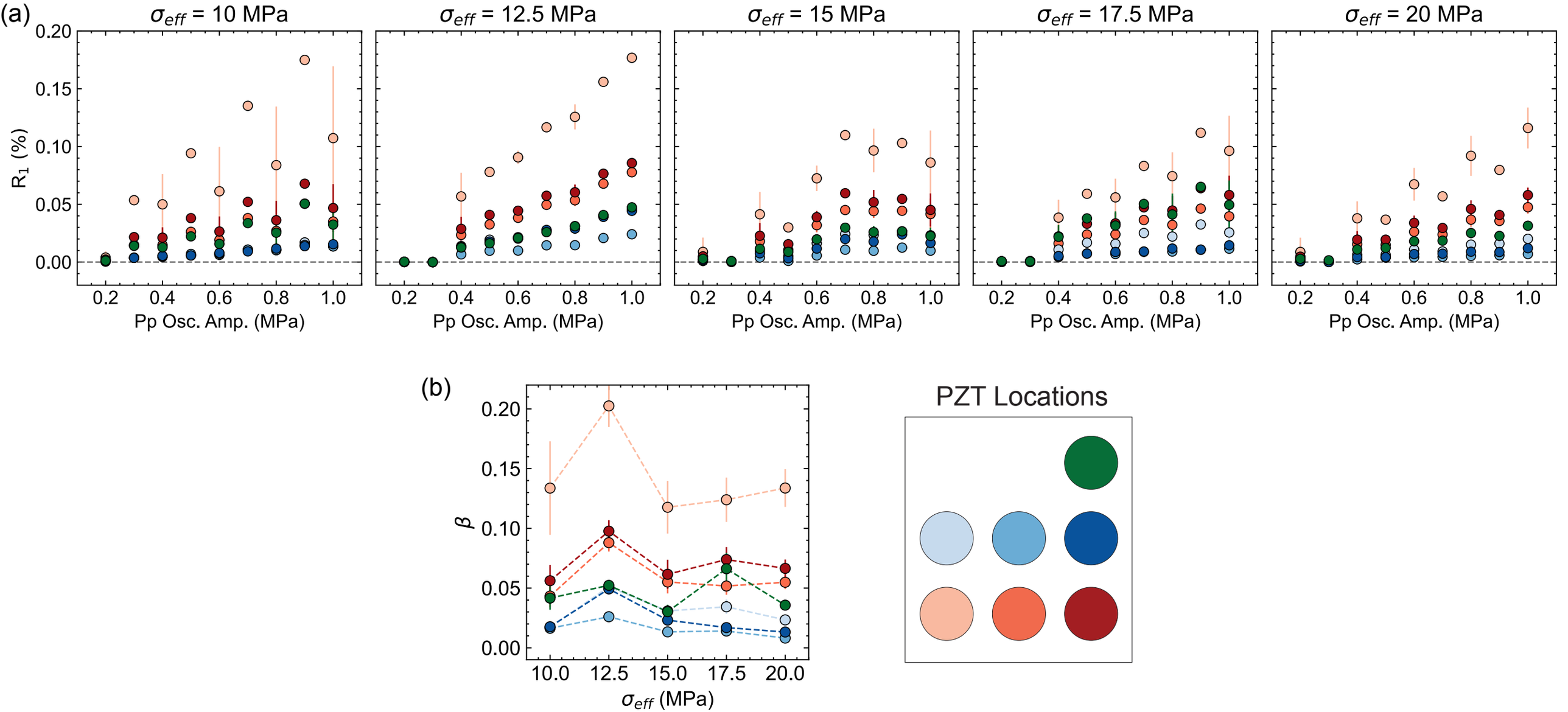
(a)
σ_{eff} = 10 MPa
σ_{eff} = 12.5 MPa
σ_{eff} = 15 MPa
σ_{eff} = 17.5 MPa
σ_{eff} = 20 MPa
R_1 (%)
0.20
0.15
0.10
0.05
0.00
0.2
0.4
0.6
0.8
1.0
Pp Osc. Amp. (MPa)
(b)
β
10.0
12.5
15.0
17.5
20.0
σ_{eff} (MPa)
PZT Locations

Figure9.

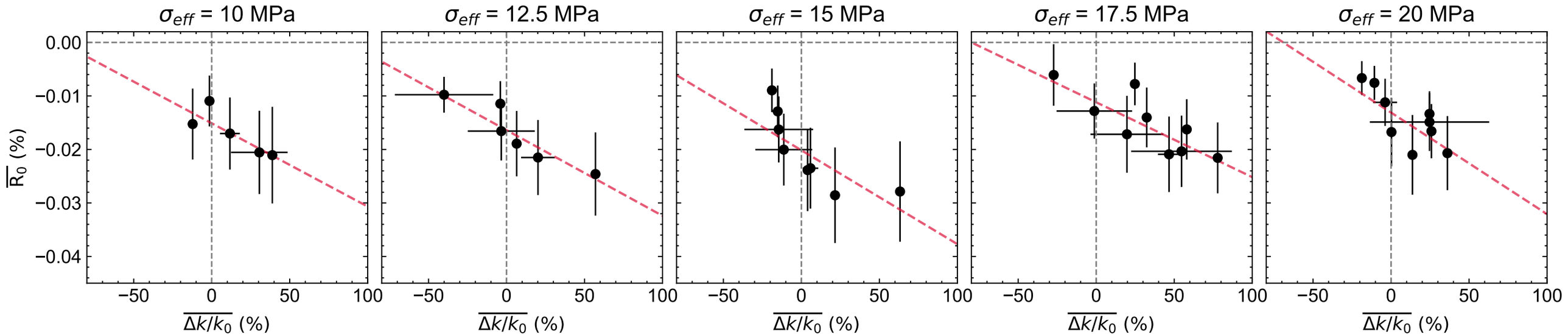
σ_{eff} = 10 MPa
σ_{eff} = 12.5 MPa
σ_{eff} = 15 MPa
σ_{eff} = 17.5 MPa
σ_{eff} = 20 MPa
$\overline{R_0}$ (%)
0.00
−0.01
−0.02
−0.03
−0.04
−50
0
50
100
$\overline{\Delta k/k_0}$ (%)

Figure10.

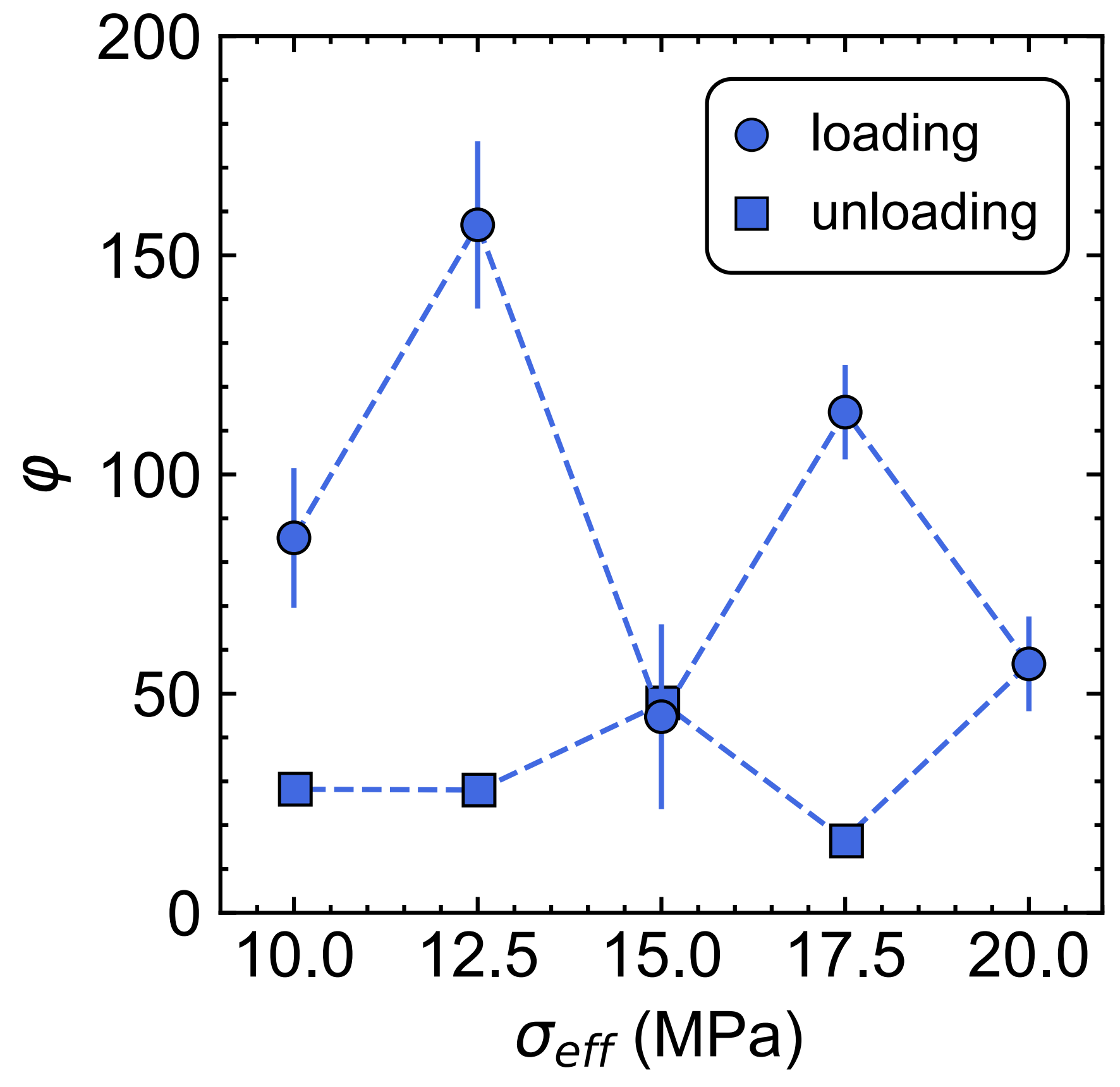
200
150
100
50
0
φ
10.0
12.5
15.0
17.5
20.0
σ_{eff} (MPa)
loading
unloading

Figure11.

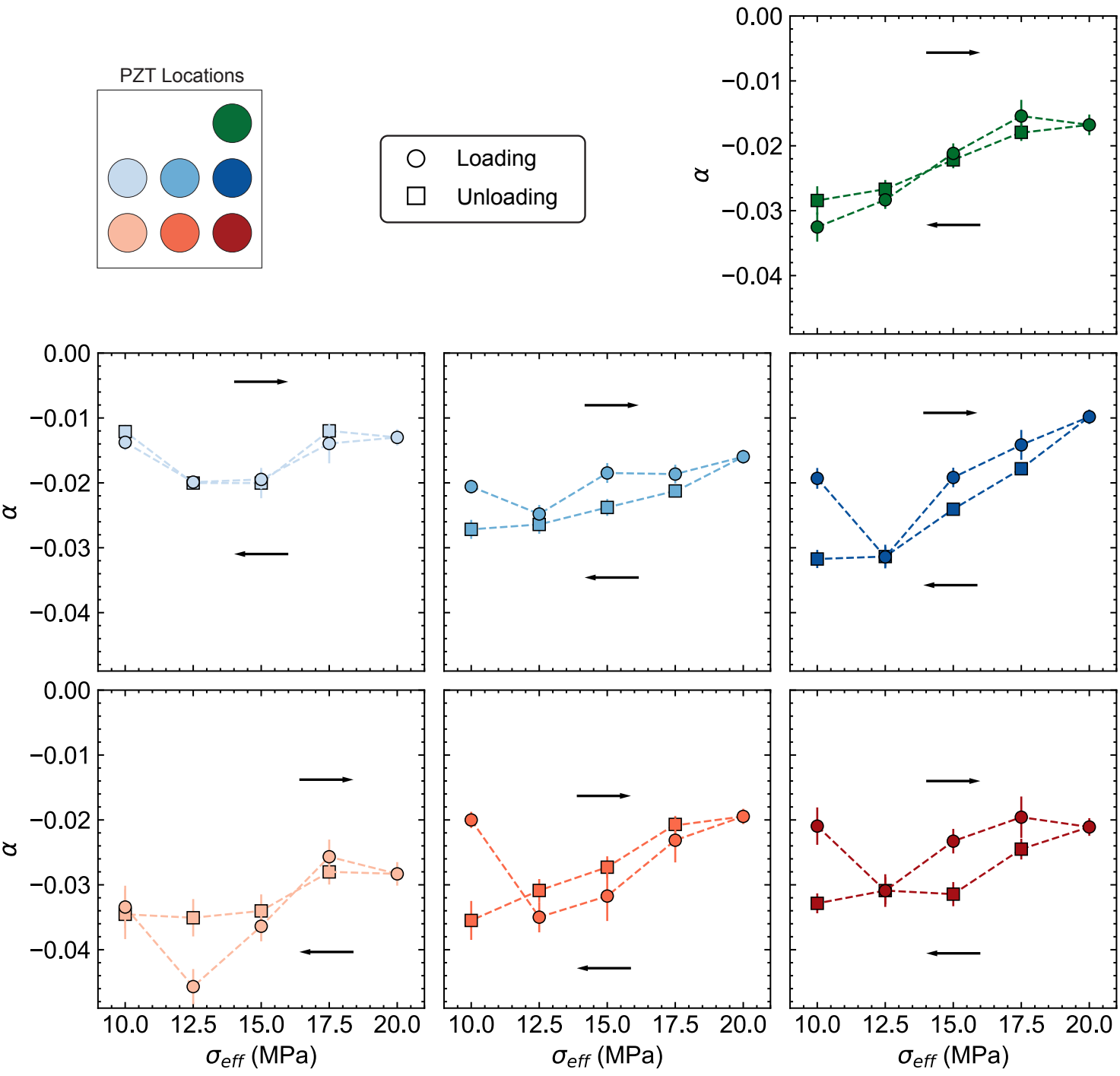
PZT Locations
Loading
Unloading
α
0.00
−0.01
−0.02
−0.03
−0.04
10.0
12.5
15.0
17.5
20.0
σeff (MPa)

Figure12.

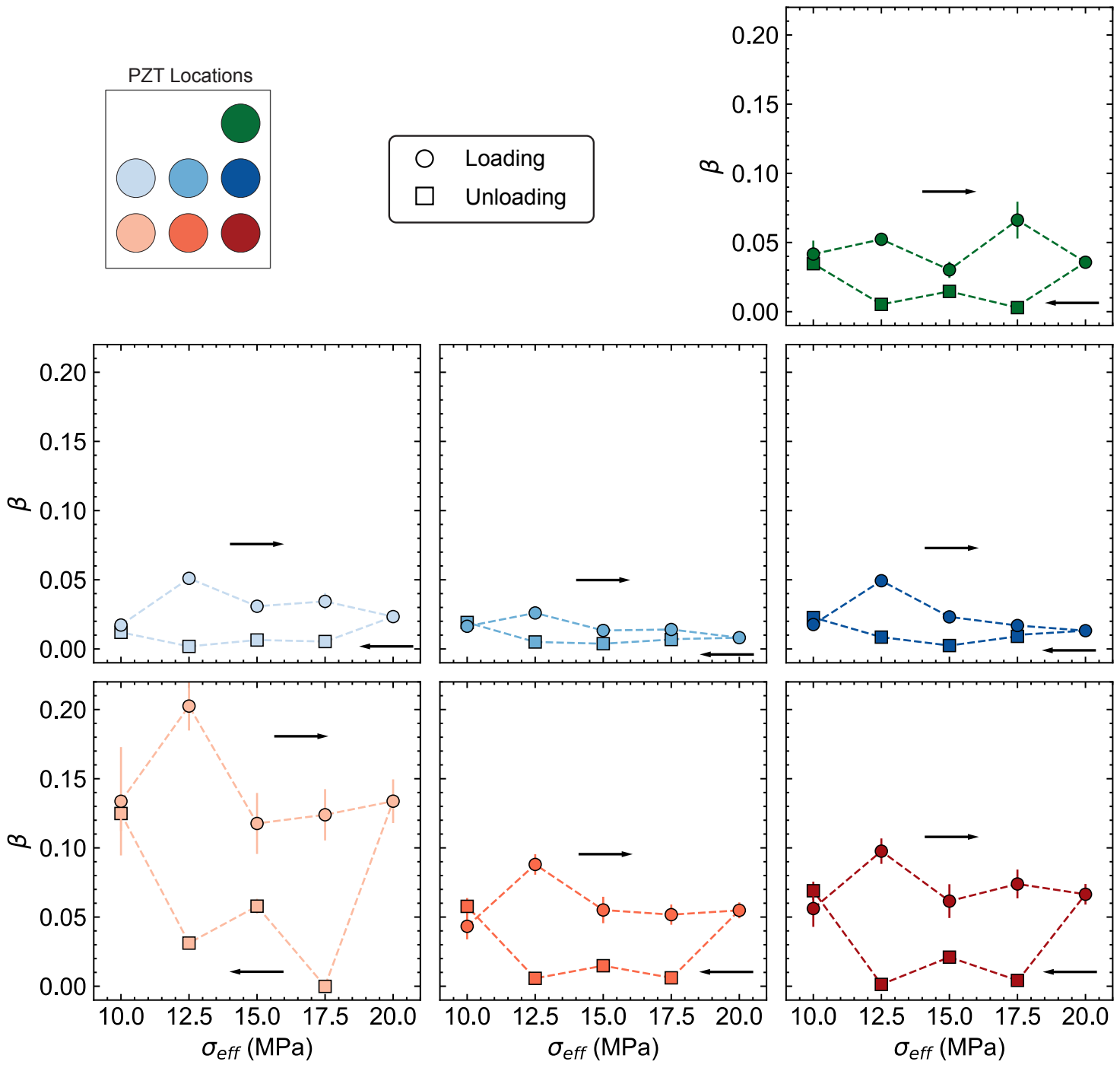
PZT Locations
Loading
Unloading
β
0.20
0.15
0.10
0.05
0.00
10.0
12.5
15.0
17.5
20.0
σeff (MPa)

Figure13.

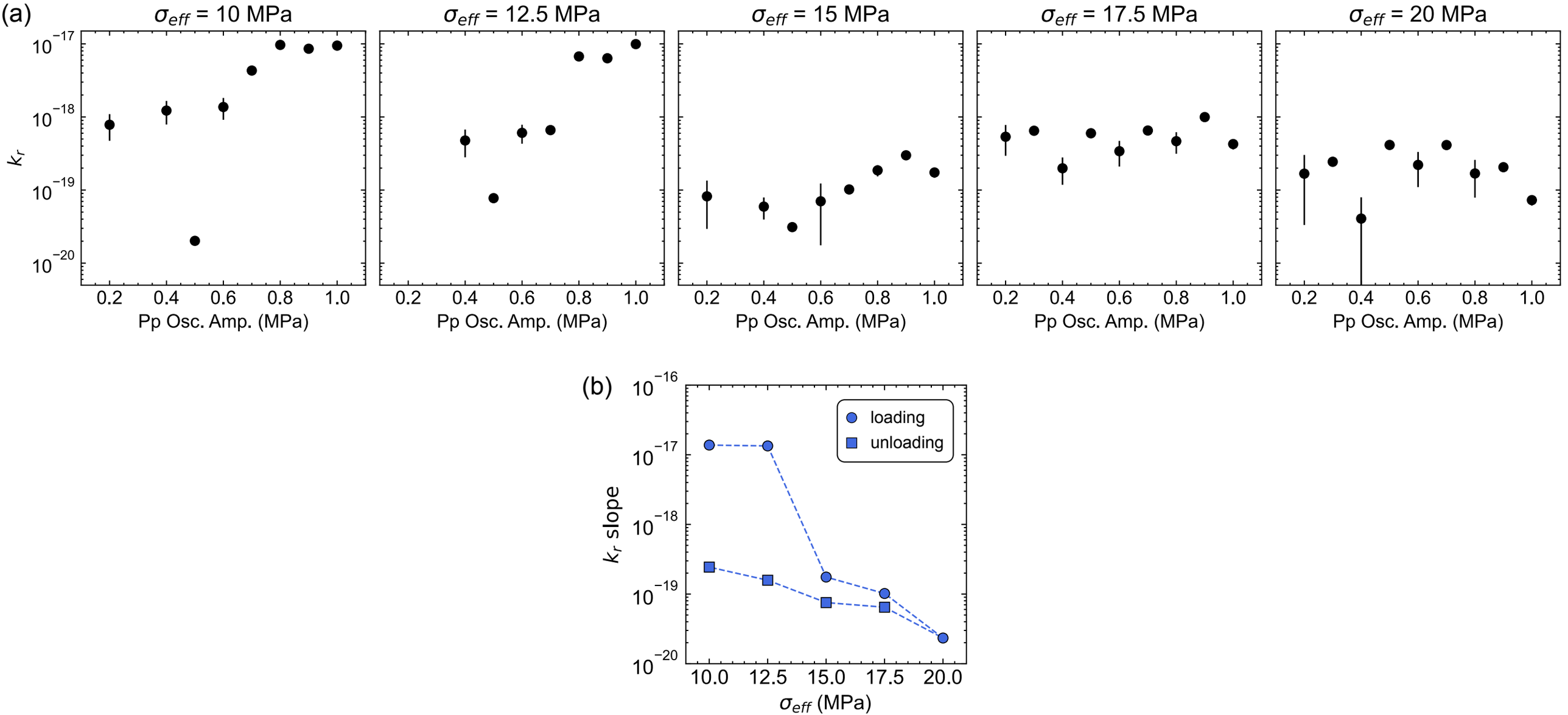
(a)
σ_{eff} = 10 MPa
σ_{eff} = 12.5 MPa
σ_{eff} = 15 MPa
σ_{eff} = 17.5 MPa
σ_{eff} = 20 MPa
k_r
10^{-17}
10^{-18}
10^{-19}
10^{-20}
0.2
0.4
0.6
0.8
1.0
Pp Osc. Amp. (MPa)
(b)
k_r slope
10^{-16}
10^{-17}
10^{-18}
10^{-19}
10^{-20}
loading
unloading
10.0
12.5
15.0
17.5
20.0
σ_{eff} (MPa)

Figure14.

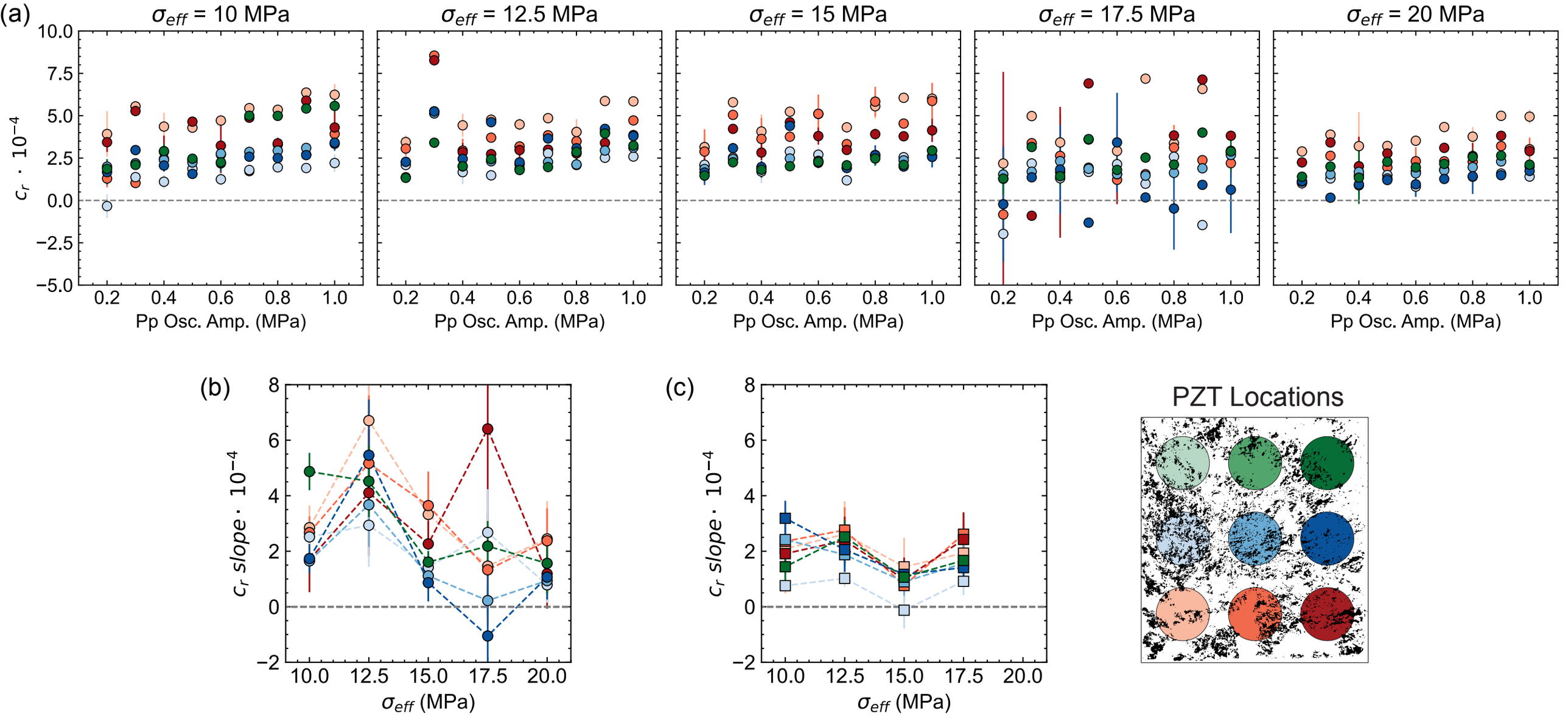
(a)
σ_{eff} = 10 MPa
σ_{eff} = 12.5 MPa
σ_{eff} = 15 MPa
σ_{eff} = 17.5 MPa
σ_{eff} = 20 MPa
$c_r \cdot 10^{-4}$
Pp Osc. Amp. (MPa)
(b)
c_r slope $\cdot 10^{-4}$
σ_{eff} (MPa)
(c)
c_r slope $\cdot 10^{-4}$
σ_{eff} (MPa)
PZT Locations

Figure15.

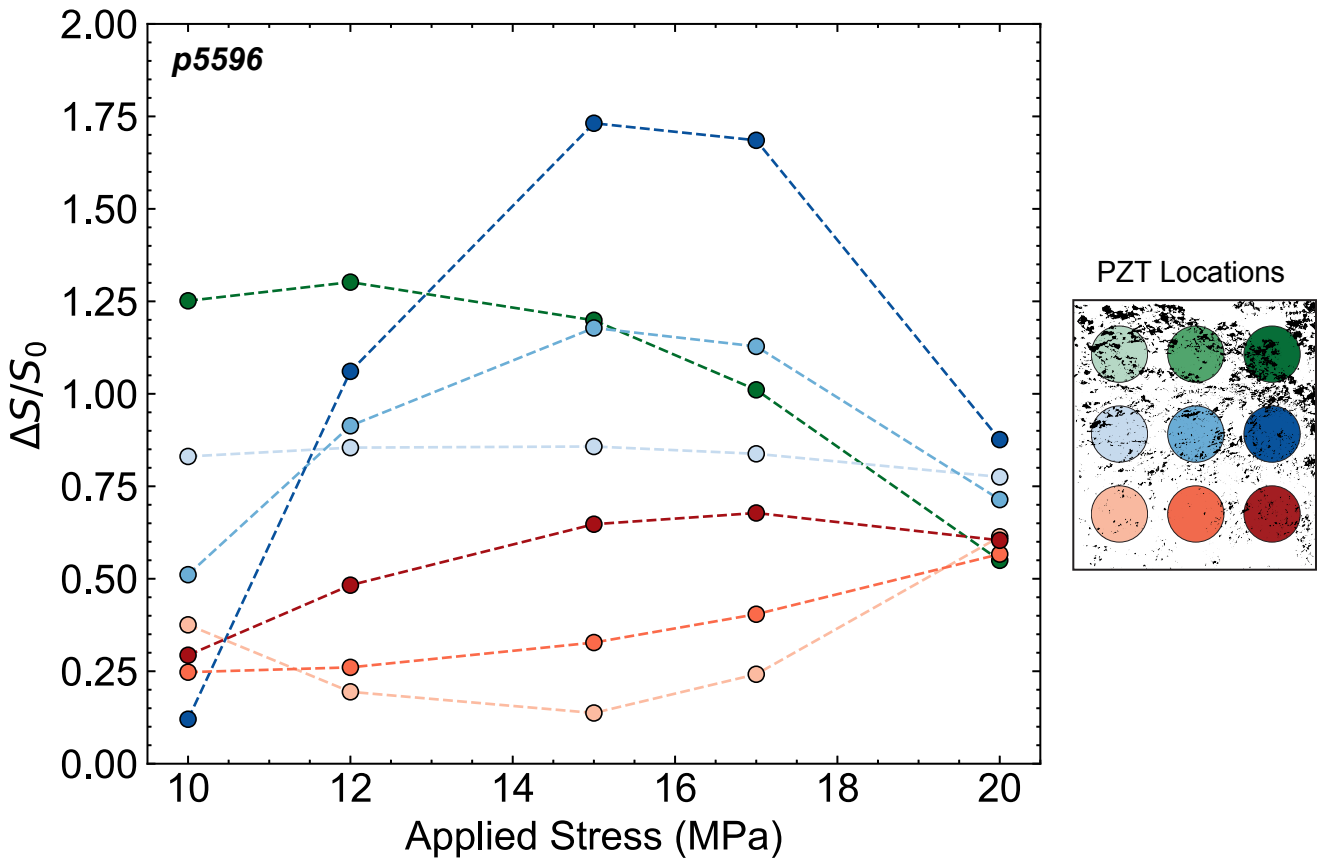
p5596
2.00
1.75
1.50
1.25
1.00
0.75
0.50
0.25
0.00
ΔS/S0
10
12
14
16
18
20
Applied Stress (MPa)
PZT Locations

Figure16.

(a)

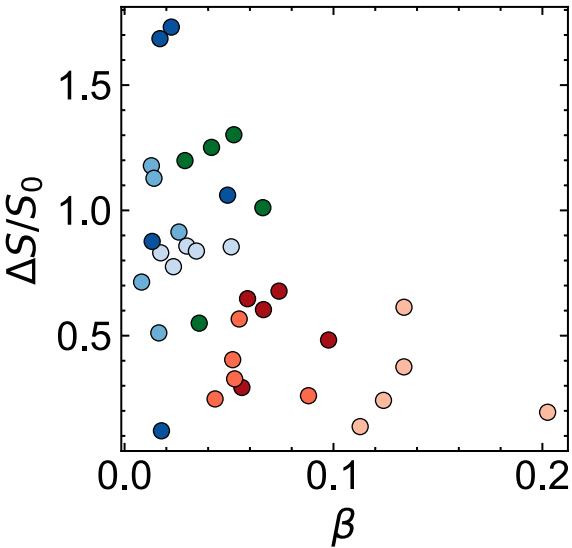

(b)

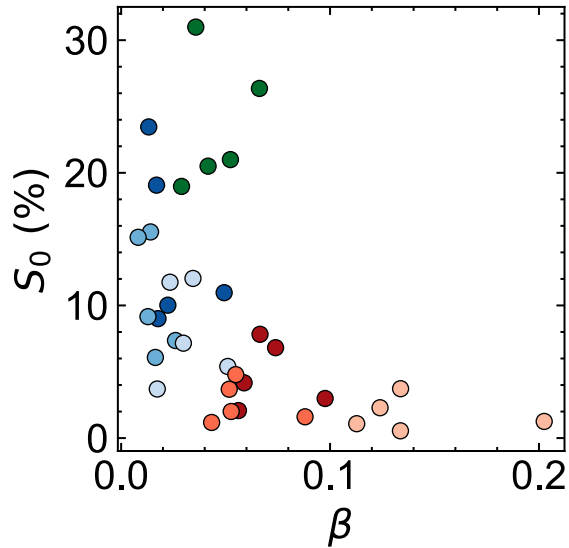

PZT Locations

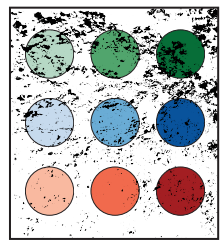

Figure17.

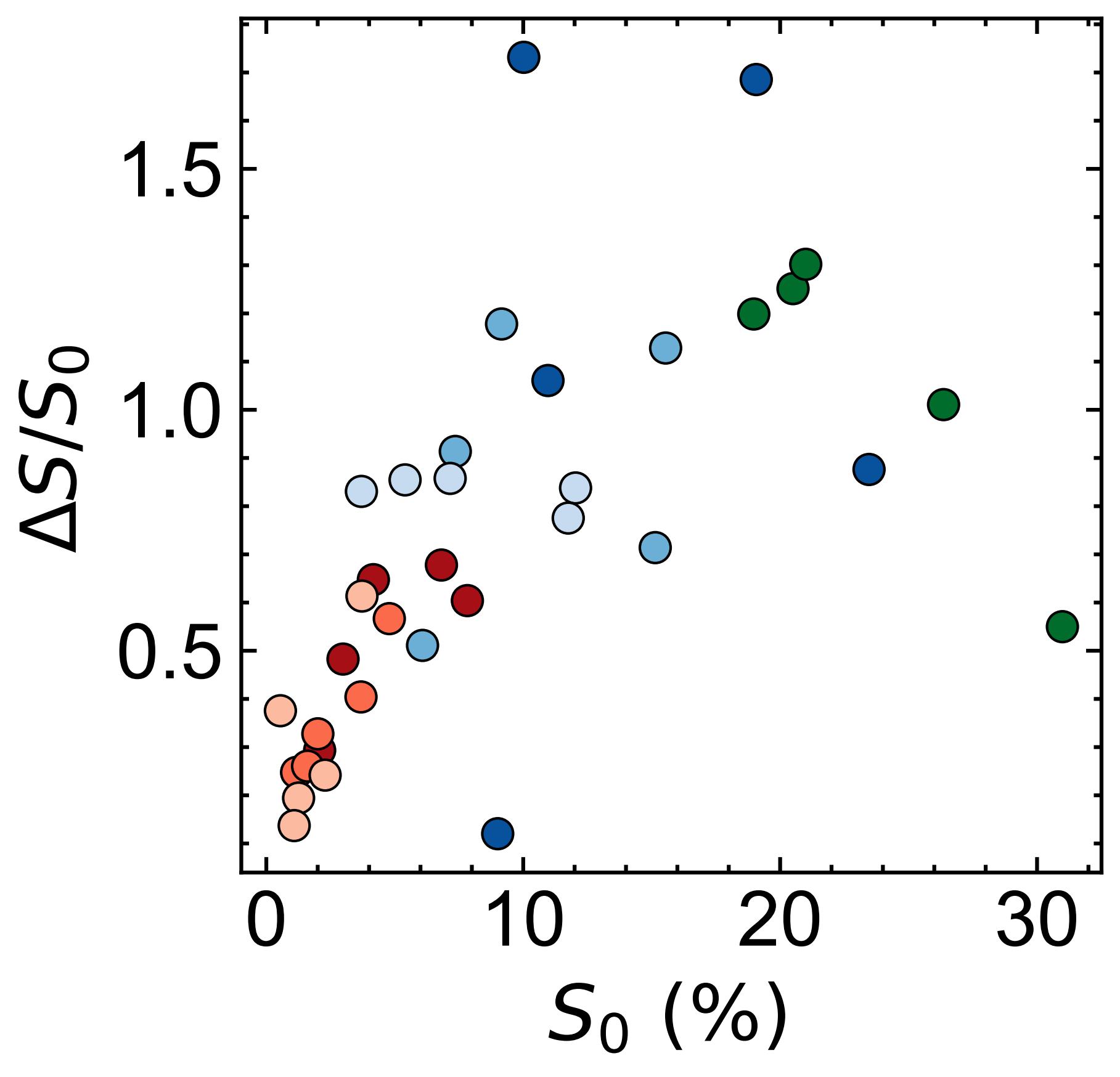
1.5
1.0
0.5
$\Delta S/S_0$
0
10
20
30
S_0 (%)